NAVAL POSTGRADUATE SCHOOL
Monterey, California

THESIS

AN INVESTIGATION OF DIURNAL VARIABILITY IN WIND AND OCEAN CURRENTS OFF HUNTINGTON BEACH, CALIFORNIA

by

Kelly E. Taylor

March 2003

Thesis Advisor:	Leslie K. Rosenfeld
Second Reader:	Carlyle H. Wash

Approved for public release; distribution unlimited

THIS PAGE INTENTIONALLY LEFT BLANK

REPORT DOCUMENTATION PAGE			Form Approved OMB No. 0704-0188
Public reporting burden for this collection of information is estimated to average 1 hour per response, including the time for reviewing instruction, searching existing data sources, gathering and maintaining the data needed, and completing and reviewing the collection of information. Send comments regarding this burden estimate or any other aspect of this collection of information, including suggestions for reducing this burden, to Washington headquarters Services, Directorate for Information Operations and Reports, 1215 Jefferson Davis Highway, Suite 1204, Arlington, VA 22202-4302, and to the Office of Management and Budget, Paperwork Reduction Project (0704-0188) Washington DC 20503.			
1. AGENCY USE ONLY *(Leave blank)*	**2. REPORT DATE** March 2003	**3. REPORT TYPE AND DATES COVERED** Master's Thesis	
4. TITLE AND SUBTITLE: An Investigation of Diurnal Variability in Wind and Ocean Currents Off Huntington Beach, California			**5. FUNDING NUMBERS**
6. AUTHOR(S) Taylor, Kelly E.			
7. PERFORMING ORGANIZATION NAME(S) AND ADDRESS(ES) Naval Postgraduate School Monterey, CA 93943-5000			**8. PERFORMING ORGANIZATION REPORT NUMBER**
9. SPONSORING /MONITORING AGENCY NAME(S) AND ADDRESS(ES) N/A			**10. SPONSORING/MONITORING AGENCY REPORT NUMBER**
11. SUPPLEMENTARY NOTES The views expressed in this thesis are those of the author and do not reflect the official policy or position of the Department of Defense or the U.S. Government.			
12a. DISTRIBUTION / AVAILABILITY STATEMENT Approved for public release; distribution unlimited			**12b. DISTRIBUTION CODE**

13. ABSTRACT ***(maximum 200 words)***

In conjunction with the Huntington Beach Phase III Investigation, the diurnal variability in the wind and ocean currents from July 1 - October 12, 2001 over the San Pedro Shelf is investigated. Results suggest that the diurnal currents are driven by the diurnal winds but that the strength of the ocean response is modulated by the low frequency flow regime. The spectral peak of the near-surface currents is at the diurnal frequency, which is below the inertial frequency (1.107 cpd). The diurnal currents are surface-intensified, decaying with depth to a minimum at 10-13 m and increasing slightly in strength below that. The near-surface diurnal currents are in phase across the shelf, and are close to in phase with the winds over the shelf. The amplitude modulation of the diurnal energy of the ocean currents is correlated with the direction of the low frequency flow along the shelf; the energy is enhanced when the flow is equatorward, and weak when the flow is poleward. The amplitudes of the diurnal near-surface currents are also correlated with the diurnal winds. However, the low frequency currents and winds are not well correlated.

14. SUBJECT TERMS diurnal variability, near-surface ocean currents, diurnal wind forcing, land-sea breeze, San Pedro Shelf			**15. NUMBER OF PAGES** 106
			16. PRICE CODE
17. SECURITY CLASSIFICATION OF REPORT Unclassified	**18. SECURITY CLASSIFICATION OF THIS PAGE** Unclassified	**19. SECURITY CLASSIFICATION OF ABSTRACT** Unclassified	**20. LIMITATION OF ABSTRACT** UL

NSN 7540-01-280-5500 Standard Form 298 (Rev. 2-89)
Prescribed by ANSI Std. 239-18

THIS PAGE INTENTIONALLY LEFT BLANK

Approved for public release; distribution is unlimited

AN INVESTIGATION OF DIURNAL VARIABILITY IN WIND AND OCEAN CURRENTS OFF HUNTINGTON BEACH, CALIFORNIA

Kelly E. Taylor
Lieutenant, United States Navy
B. S., United States Naval Academy, 1997

Submitted in partial fulfillment of the
requirements for the degree of

MASTER OF SCIENCE IN METEOROLOGY AND OCEANOGRAPHY

from the

NAVAL POSTGRADUATE SCHOOL
March 2003

Author:

Kelly E. Taylor

Approved by:

Leslie K. Rosenfeld
Thesis Advisor

Carlyle H. Wash
Second Reader

Mary Batteen, Chairman
Department of Oceanography

THIS PAGE INTENTIONALLY LEFT BLANK

ABSTRACT

In conjunction with the Huntington Beach Phase III Investigation, the diurnal variability in the wind and ocean currents from July 1 - October 12, 2001 over the San Pedro Shelf is investigated. Results suggest that the diurnal currents are driven by the diurnal winds but that the strength of the ocean response is modulated by the low frequency flow regime. The spectral peak of the near-surface currents is at the diurnal frequency, which is below the inertial frequency (1.107 cpd). The diurnal currents are surface-intensified, decaying with depth to a minimum at 10-13 m and increasing slightly in strength below that. The near-surface diurnal currents are in phase across the shelf, and are close to in phase with the winds over the shelf. The amplitude modulation of the diurnal energy of the ocean currents is correlated with the direction of the low frequency flow along the shelf; the energy is enhanced when the flow is equatorward, and weak when the flow is poleward. The amplitudes of the diurnal near-surface currents are also correlated with the diurnal winds. However, the low frequency currents and winds are not well correlated.

THIS PAGE INTENTIONALLY LEFT BLANK

TABLE OF CONTENTS

THIS PAGE INTENTIONALLY LEFT BLANK

LIST OF FIGURES

THIS PAGE INTENTIONALLY LEFT BLANK

LIST OF TABLES

THIS PAGE INTENTIONALLY LEFT BLANK

ACKNOWLEDGMENTS

I would like to thank Mike Cook and Todd Anderson for assisting with data processing. I would like to thank Fred Bahr for assisting with data processing, assimilation, and display. Professor Rosenfeld was funded by Orange County Sanitation District.

I gratefully thank my entire family for supporting me during the long hours I have spent away from home while finishing this thesis. I am especially indebted to my advisors, Professor Leslie Rosenfeld and Professor Chuck Wash. Without Professor Rosenfeld's patience, understanding, knowledge, organizational skills and her pursuit of excellence, and Professor Wash's wealth of experience, this thesis would have never been completed.

THIS PAGE INTENTIONALLY LEFT BLANK

I. INTRODUCTION

A. MOTIVATION

One of the processes affecting coastal ocean environments is the offshore discharge of municipal wastewater, which has been regulated by the Federal Clean Water Act since 1972. On the West Coast, and particularly Southern California, this method of removal is used in conjunction with the narrow continental shelves and steep continental slope, facilitating the diffusion of the effluent. The effluent leaves the outfall system as a buoyant plume, and is then subject to local oceanic processes, such as local current regimes, density stratification, and bottom topography, all of which interact in a complex nature that is poorly understood (Washburn et al., 1992).

The goal of any sanitation district is to minimize the effect of the wastewater discharge on the environment, in compliance with the Federal Clean Water Act. Orange County Sanitation District (OCSD) is one of the largest districts in the country, and as such has instituted a comprehensive ocean-monitoring program to examine the effect of their outfall system, if any, on the surrounding marine environment. The program consists of three components: a long-term core study, a strategic process study, and regional monitoring, which includes a larger geographical area (OCSD, 2001). The areas of Huntington and Newport Beaches, which are within a few kilometers of the OCSD outfall, have been subject to closure and postings for certain periods of time over the past several years due to bacterial levels exceeding the acceptable limit. The Strategic Process Study (SPS) of the Ocean Monitoring Program specifically focuses on the oceanographic processes affecting the dilution of the effluent using both in-situ and ship-based surveys (SAIC, 2001). The overall goal of Phase III of the Huntington Beach Investigation is determining whether there exists a mechanism for transport of the offshore wastewater plume into the nearshore environment.

Though many different theories are being investigated as possible transport mechanisms, the objective of this study is to provide a better understanding of the effect of diurnal wind forcing on coastal ocean circulation, with an eye to quantifying this possible mechanism for transport of the OCSD wastewater outfall plume into the

shoreline. Few other studies attempting to correlate the diurnal wind stress and ocean currents have been conducted. The first integrated study used the Coastal Ocean Dynamics Experiment (CODE) data of the summers of 1981 and 1982 off the continental shelf of Northern California, and examined the contributions made by tidal and atmospheric forcing to the diurnal period current fluctuations. Results indicate low frequency equatorward wind stress is accompanied by a strong diurnal signal in the alongshelf component of wind stress. The combination of direct forcing by the local diurnal wind stress as well as the diurnal heating cycle account for the majority of diurnal period energy observed in the upper ocean currents over the inner and mid shelf (Rosenfeld, 1988). Another study focuses on internal waves driven by diurnal wind forcing using the Internal Waves on the Continental Margin (IWAVES) data collected off Mission Beach, California during 1996 and 1997. Motions are surface enhanced, clockwise circularly polarized and have an upward phase propagation speed of ~68 m d^{-1}, suggesting they are driven primarily by the diurnal sea breeze; however, they are much more intermittent in time than would be expected if associated with the diurnal forcing of the sea breeze (Lerczak et al., 2001).

Though the Huntington Beach study focuses on a public health concern, the characterization of the flow in coastal oceans also has relevance to military applications. In particular the timing of littoral operations depend upon the strength of the wind and currents, which vary diurnally.

B. BACKGROUND

1. Large-Scale Description of the Southern California Bight

The Southern California Bight (SCB) is the region that extends south from the sharp bend in the California coastline at Point Conception to San Diego. The bight is dominated by the offshore equatorward flowing California Current system, and that portion of the California Current that turns inshore and poleward and recirculates within the bight is known as the Southern California Eddy (Figure 1). A poleward flowing undercurrent, which transports warmer, saltier Equatorial water from the south also dominates the inshore region, and is strongest at depths of 100-300 m (Hickey 1998,

1992; Lynn and Simpson, 1987). The ocean circulation within the bight has a markedly seasonal variation: maximum poleward flow in both the summer and winter, associated with the maximum in the California Current and Undercurrent and the surfacing of the undercurrent, respectively, and minimum poleward flow in the spring (Hickey, 1992, Bray et al., 1999). While the California Current System, which extends from the Straights of Juan de Fuca to the tip of Baja California, is dominated by certain physical environmental characteristics such as strong wind stress forcing, large influence of bottom topography, and large alongshore atmospheric and oceanographic scales, the Southern California Bight differs significantly (Hickey, 1998).

Bottom topography within the bight is extremely complex, and varies from north to south. Offshore islands and ridges surrounded by deep basins, as well as an irregular coastline interrupted by submarine canyons, add to the intricacies in the flow field. The shelf, though overall more narrow (2-5 km) than the average shelf of the West Coast of North America (~ 40 km), is subject to many discontinuities, composed of both narrow regions to the south and wider partially enclosed shelves to the north (Hickey, 1998). In areas of shallow topography such as near the coast, flow tends to follow the isobaths, conserving vorticity. The scale of along-isobath flow not only depends on the scale of the isobaths themselves, but also on the stratification (Gill, 1982). In her analysis of the Santa Monica-San Pedro Basin, Hickey (1992) has also found that as the sea floor is approached, flow becomes more aligned with local topography, and larger topographic scales become more influential as the distance from the sea floor increases.

The winds along the west coast of the US are governed primarily by the location of the Eastern Pacific Subtropical High, which dominates the large-scale wind field in the summer, and migrates southeastward in the winter, while low pressure dominates the northern Pacific. The wind direction is equatorward along the entire coast during summer, but reverses direction north of San Francisco during winter. Maximum equatorward wind stress occurs during the spring in southern California, and during the summer in northern California, while minimum equatorward stress occurs during late fall and winter (Hickey, 1998). As Hickey (1992) shows, mean monthly winds within the Southern California Bight, derived from NDBC buoy 46025, are southwesterly and significantly reduced compared to the model-derived northwesterly winds in the region

north of the bight. Winant and Dorman (1997) find that during spring and summer, winds in the bight are usually weak and directed onshore; monthly mean wind stresses are less than the standard deviation along the major axis. Wind stress increases with distance from the coast during all seasons, though the seasonally averaged wind stresses are stronger during spring and summer than during fall and winter. Coincidentally, the largest gradients in the wind stress fields occur in the spring.

The strongest upwelling-favorable winds within the bight occur in winter and early spring, which appear to be driven by the large-scale winds. Though upwelling favorable winds still occur within the bight during summer and fall, their amplitude is appreciably damped. Therefore, local upwelling is generally seen in the winter and spring, and generally absent during summer and fall, though upwelled waters north of Point Conception are commonly advected into the bight region through the Santa Barbara Channel (SBC). The probable result of the reduced wind stress and complex basin topography in the bight is wind driven signals with much smaller along-shelf scales and smaller shorter-than-seasonal current fluctuations than to the north of the bight (Hickey, 1998).

Several studies have been done in an attempt to characterize the forcing mechanisms responsible for the seasonal flow in the bight (Hickey 1992, 1998; Hickey et al., 2003, Bray et al., 1999), yet in characterizing the seasonal flow, there is still a great degree of mesoscale variability within the area that adds to the complexity. Poleward flow in summer is credited to an increase in the alongshore pressure gradient (APG) (Hickey and Pola, 1983, cited in Bray et al., 1999), and an increase in wind stress curl (McCreary et al., 1987, cited in Bray et al., 1999). In a 1999 study, Bray et al. find positive wind stress curl everywhere within the bight, which explains poleward flow within the bight in terms of Sverdrup balance. They also find upward phase propagation of seasonal currents in the Eastern Santa Barbara Channel. This upward phase propagation possibly indicates poleward propagation of a remotely generated wind signal, which would account for some of the seasonal variation in currents in the bight. Hickey et al. (2003) have completed a study on the Santa Monica-San Pedro Basin and accredit the long period fluctuations (10-25 d) responsible for a majority of the velocity variance over the shelf and slope of the central SCB to disturbances originating

equatorward of the bight. Evidence supporting this includes offshore and upward phase propagation of velocity disturbances over the slope, and maximum correlation with currents, sea level and APG with wind stress several hundred kilometers equatorward of the bight.

The annual average sea temperature within the SCB is not as cold as the sea temperature elsewhere along the West Coast. The mean sea temperature is colder in the northern bight and warmer in the southern bight (Hickey, et al., 2003). As previously mentioned, local upwelling is strongest in winter and spring, and generally absent during summer and fall. Colder water is commonly advected into the bight through the SBC; thus, minimum sea temperature occurs near Point Conception in April. Sea temperature patterns within the bight correspond to the air temperature, with sea temperature generally exceeding the air temperature by 1^{o}C in all seasons (Winant and Dorman, 1997). Hickey et al. (2003) also find long period temperature fluctuations (10-25 d) in the study of the Santa Monica Basin-San Pedro Shelf. These fluctuations are attributed to propagating APGs, which produce currents that transport heat in lateral directions along the coast. In nearshore regions, to distinguish these lateral advection temperature changes from local upwelling, they cite a much slower time rate of change for the former, and an in-phase correlation with local alongshore wind stress for the latter.

2. Diurnal Variability

The diurnal variability in nearshore regions of the oceans is a result of a combination of forcing mechanisms, which includes tides, diurnal heat flux, and the diurnal sea breeze. It is the interaction of these forces in the presence of lower frequency variability that produce temporal and spatial fluctuations in local temperature and currents. The strength of each of the respective forces will influence its effect on the change. For example, the amount of cloud cover over a particular location will determine the amount of long and short wave radiation exchanged with the sea surface, and therefore affect the temperature of the upper water column. The strength of the diurnal sea breeze will also have some effect on the depth of the surface mixed layer; a strong sea breeze resulting in a deeper mixed layer and a weaker sea breeze resulting in a shallower mixed layer. The sea breeze will also evoke a lagged response in the surface currents.

Hickey (1998) discusses the nature of the tidal currents along the West Coast. The barotropic tides are mixed, but predominantly semidiurnal. The internal tidal currents, also predominantly semidiurnal, are typically larger than the barotropic tidal currents (5-10 cm s^{-1} vs. < 5 cm s^{-1}, respectively). Variance due to barotropic tidal currents generally account for a small amount of the high-frequency variance in the currents. Baroclinic tidal currents do not usually dominate the alongshelf current variance, but can dominate the weaker cross-shelf currents. Barotropic tidal ellipses are rectilinear and oriented along the local bathymetry.

The sea breeze is a well-documented and understood mesoscale occurrence in coastal regions. It arises due to pressure differences created by differential heating and cooling of the land and sea on a daily cycle. During the day, the sea breeze develops as the land heats and air rises, creating low pressure. The colder air over the ocean flows toward land to replace the rising air. The opposite occurs during the night, when the land cools faster than the ocean, and high pressure develops. The colder air over the land sinks and flows toward the ocean, creating the land breeze. In most places, the land-sea breeze is oriented perpendicular to the coast, though in the late afternoon it may be turned parallel to the coast (rotated clockwise in the Northern Hemisphere) due to the effect of the Coriolis force and friction. The sea breeze is generally stronger than the land breeze, for a number of reasons. The air is less stably stratified during the day, a deeper layer of air is heated during the day than is cooled at night, and friction has a much smaller effect on the sea breeze. The diurnal sea breeze may also be modified by a number of factors, such as synoptic scale winds, adjacent topography, shape of the coastline, and the type of land adjacent to the coastal ocean. All of these will have an effect on the strength and penetration of the diurnal sea breeze.

As previously mentioned, diurnal wind-forcing of the ocean currents is not a well-studied phenomenon, with the exception of the studies noted and the concurrent investigation of this data set (Hamilton, 2003). Rosenfeld (1988) finds that off northern California, the diurnal variability in the alongshelf component of the wind is greater than the cross-shelf component. The diurnal period currents are intermittent in time, surface-intensified and clockwise rotating. The near-surface currents reach maximum speeds at approximately the same time as the wind stress, and the phase of the currents decreases

with depth. The results of the study indicate a strong correlation between the amplitude modulation of the diurnal currents at depths up to 20 m and the amplitude modulation of the alongshelf wind stress. Correlations are greatest between the currents at any given mooring and the wind stress at that same mooring, and correlations are highest near the coast and at the surface, decreasing with distance offshore and depth.

In their study off Mission Beach, California, Lerczak et al. (2001) discuss surface-enhanced, clockwise polarized, intermittent currents. The inertial frequency at this site is 1.08 cpd, but the variance of the currents is peaked at the diurnal frequency (1 cpd). The wind is generally weak, with a sharp spectral peak at 1 cpd. The diurnal peak in the ocean is much broader than the sharp diurnal peak in the wind. The diurnal currents penetrate well below the mixed layer and have consistent upward phase propagation, which is not expected for subinertial motions. They feel this implies that low-frequency background currents play an important role in priming the ocean's response to diurnal wind forcing by altering the relative vorticity of the current field, which at times changes the effective Coriolis parameter such that the diurnal frequency goes from being subinertial to superinertial.

3. Internal Wave Theory

Though the understanding of the exact generation mechanism of linear internal waves is incomplete, the theory governing their motion is well understood and widely used. The simplest way internal waves can be comprehended is to compare them to surface gravity waves, but on the interface between two layers of fluid with different densities, rather than at the air-sea interface. The density differences in the water column are much smaller than the density differences between water and air. The restoring force for gravity waves is proportional to gravity times the density differences between the two layers upon which the wave exists. In the case of internal waves, the acceleration due to gravity is $g' = g\frac{\Delta\rho}{\rho}$, vice g, and so it is g' that determines the pressure differences (Gill, 1982). When a fluid parcel at its equilibrium position is disturbed, it experiences this restoring force and propagates as a wave. Due to the small difference in densities, internal waves have a much longer period and wavelength than surface waves. Internal waves also have much slower phase speeds than surface gravity waves, due to $g' << g$.

The displacement at the interface between the two layers of fluid is also larger than the displacement at the sea surface. A two-layer system gives rise to two modes of variability, the barotropic (or external) mode, and the baroclinic mode. In the case of the barotropic mode, the surface displacement is comparable to the interface displacement, and the water parcel velocities are the same in both layers. In the case of the baroclinic mode, the surface displacements are small compared with the interface displacements, and the water parcel velocities are opposite in the two layers.

The real ocean is, of course, continuously stratified, which gives rise to some unique characteristics when internal waves are present. In a continuously stratified medium, internal waves can propagate both vertically and horizontally. This behavior makes internal waves extremely important because they represent a way for energy to propagate from the bottom to the surface of the ocean, and vice versa. This behavior can be described using the dispersion relation for internal waves, defined as

$$\omega^2 = \frac{f^2 m^2 + N^2 (k^2 + l^2)}{k^2 + l^2 + m^2} \tag{1}$$

where $f = 2\Omega \sin \Phi$, which is the inertial frequency and depends on the rotation rate of the earth (angular frequency Ω) and the latitude of interest, Φ. The horizontal components of the wavenumber vector are *k* and *l*, and the vertical component is *m*. $N = \sqrt{\frac{-g}{\rho_o}\frac{\partial \rho}{\partial z}}$, which is known as the Brunt-Vaisala or buoyancy frequency, is a measure of the strength of stratification and is depth-dependent. If a fluid is strongly stratified, vertically displaced parcels will experience a larger restoring force. Using θ to denote the angle between the wavenumber vector and the horizontal plane, equation (1) can be written as

$$\cos^2 \phi = \frac{\omega^2 - f^2}{N^2 - f^2} \tag{2}$$

This equation demonstrates that internal waves are confined to a frequency band between f and N, where f is the minimum frequency and N is the maximum frequency

between which internal waves may propagate freely. For internal waves at the inertial frequency f, water parcel motions are horizontal rotations, and for internal waves at the buoyancy frequency, water parcel motions are purely vertical oscillations, perpendicular to the density surfaces. For intermediate frequencies, the water parcels move in elliptical orbits. The inertial frequency at the HB study site is 1.107 cpd, which corresponds to an inertial period of 21.68 hours.

The unique characteristics of internal waves involve the direction of phase propagation and the direction of energy propagation, and their relation to the wavenumber vector. The wavenumber vector, $\vec{k}$, points in the same direction as the phase velocity, $\vec{C}_p$, which is the direction the wave crests propagate. The energy of the internal wave, however, travels at the group velocity $\vec{C}_g$, at a 90^o angle to the phase velocity. The angle between the horizontal axis and the direction of $\vec{C}_p$ (phase velocity) is defined here as ϕ (Figure 2). The water parcel motion for internal waves is along the crests and troughs, parallel to the group velocity and perpendicular to the direction of phase propagation. The sense of direction for the vertical components of the phase and group velocities are opposite one another. Therefore, upward group velocity implies downward phase velocity, and vice versa (Figure 2). Internal tides are generated by the interaction of barotropic motions with sloping bottom topography, which is found directly south-southwest of the HB study area. As the onshore tides travel up the continental slope, they may set off vertical displacements in the pycnocline.

THIS PAGE INTENTIONALLY LEFT BLANK

II. DATA COLLECTION

A. MOORED

1. Ocean Data

As part of the Huntington Beach Phase III Strategic Process Study (HB Ph III SPS), moorings were deployed at twelve locations outside the surfzone on the San Pedro Shelf for a period spanning the middle of June until the middle of October 2001 (Figure 3). Several different scientific teams maintained these moorings, including Science Applications International Incorporated (SAIC), U.S. Geological Survey (USGS), the Naval Postgraduate School (NPS), and Scripps Institute of Oceanography, who maintained several moorings very near shore. Of these locations, data from M01 and M08 are not used in the analysis presented here because of their extreme shallowness and large distance from shore, respectively. Mooring 04 was never deployed, and does not appear in the list of moorings. Locations of oceanographic and meteorological observation stations are given in Tables 1 and 2, respectively (Note HB and M may be used interchangeably). Each station includes one or more moorings supporting various instruments, measuring temperature and currents, with temporal resolution of 1 to 5 minutes, at multiple depths in the water column (Figure 4). Station 07 includes a surface mooring with the meteorological station recording winds at a sampling rate of 1 minute. Moorings 02, 03, 05, 06, and 07 are in a straight line extending perpendicular from the coast to 7 km off shore, where the depth of water is approximately 60 m. M2 is closest to shore, and M7 is furthest from shore. Moorings 09, 10, and 11 extend along a straight line at a finite angle from Moorings 02-07 toward the south-southeast, to give an indication of down-coast variability. M12 is located at the head of the OCSD outfall diffuser pipe in approximately 62 m of water, and M13 is located at the head of the Newport Canyon in approximately 15 m of water.

Mooring	Latitude	Longitude	Instrument Type	Parameter Measured	Instrument Depth (m)	Start Time	Stop Time
M02	33°37.764'N	117°58.998'W	MicroCat	Temperature	12.3	6/29/2001	10/22/2001
M03a	33°37.560'N	117°59.206'W	MicroCat	Temperature	5, 10	6/14/2001	10/12/2001
M03b	33°37.598'N	117°59.227'W	1200 kHz ADCP	Current	13.7	6/14/2001	10/12/2001
			SeaCat	Temperature	14	6/14/2001	10/12/2001
M05a	33°36.710'N	117°59.802'W	MicroCat	Temperature	5	6/13/2001	10/12/2001
			Temp	Temperature	10	6/13/2001	10/12/2001
M05b	33°36.719'N	117°59.704'W	MicroCat	Temperature	15, 20	6/14/2001	10/12/2001
M05c	33°36.745'N	117°59.822'W	600 kHz ADCP	Current	23.2	6/14/2001	10/12/2001
			SeaCat	Temperature	23.6	6/14/2001	7/23/2001
M06a	33°35.674'N	118°00.571'W	Hugrun	Temperature	1	6/26/2001	10/22/2001
			MicroCat	Temperature	5, 15, 20, 30	6/26/2001	10/22/2001
			S4	Temperature, Current	10, 28	6/26/2001	10/22/2001
M06b	33°35.667'N	118°00.423'W	300 kHz ADCP	Current	32.5	6/30/2001	10/22/2001
			Hugrun	Temperature	34.6	6/30/2001	10/22/2001
M07a	33°34.593'N	118°01.256'W	SeaCat	Temperature	5, 10	6/15/2001	10/12/2001
M07b	33°34.606'N	118°01.156'W	Temp	Temperature	15, 25, 35, 45, 50	6/14/2001	10/12/2001
			MicroCat	Temperature	20, 30, 40, 55	6/14/2001	10/12/2001
M07c	33°34.652'N	118°01.137'W	300 kHz ADCP	Current	56.9	6/14/2001	10/30/2001
			SeaCat	Temperature	57.5	6/14/2001	10/30/2001
M09	33°36.651'N	117°58.947'W	Hugrun	Temperature	1, 21	6/29/2001	10/23/2001
			MicroCat	Temperature	4, 10	6/29/2001	10/23/2001
			S4	Temperature, Current	5, 15	6/29/2001	10/23/2001
M10a	33°35.700'N	117°58.097'W	Hugrun	Temperature	1, 34.6	6/27/2001	10/23/2001
			MicroCat	Temperature	5, 15, 20, 30	6/27/2001	10/23/2001
			S4	Temperature, Current	10, 28	6/27/2001	10/23/2001
M10b	33°35.704'N	117°57.952'W	300 kHz ADCP	Temperature, Current	35	6/14/2001	10/12/2001
M11a	33°34.792'N	117°57.615'W	Temp	Temperature	5	6/13/2001	10/17/2001
			MicroCat	Temperature	10	6/13/2001	10/30/2001
M11b	33°34.784'N	117°57.660'W	Temp	Temperature	15, 25, 35, 45	6/14/2001	10/12/2001
			MicroCat	Temperature	20, 30	6/13/2001	10/12/2001
M11c	33°34.812'N	117°57.551'W	300 kHz ADCP	Current	50.7	6/13/2001	10/30/2001
			SeaCat	Temperature	51.5	6/13/2001	10/30/2001
M12	33°34.366'N	118°00.112'W	DCS-3900	Temperature, Current	1, 45	6/28/2001	10/13/2001
			Therm	Temperature	15, 30, 48	6/28/2001	10/13/2001
			Hugrun	Temperature	61	6/28/2001	10/13/2001
M13	33°36.220'N	117°56.331'W	Hugrun	Temperature	1, 14.2	6/30/2001	10/23/2001
			FSI/Hugrun	Temperature, Current	5	6/30/2001	10/23/2001
			SeaCat	Temperature	8	6/30/2001	10/23/2001

Table 1. Oceanographic data used in thesis research.

Due to variations in the period of collection time for the data associated with each of the instruments, a common start and stop time of July 1, 2001 to October 12, 2001 is chosen for the time series of temperature, wind and ocean currents, in order to make quantitative comparisons. Instruments used to collect ocean current data include the InterOcean S4 Electromagnetic Current Meter, Falmouth Scientific (FSI) 2D-Acoustic

Current Meter (ACM), Aanderra Doppler Current Sensor DCS-3900 (which also records ocean temperature), and RD Instruments WorkHorse Acoustic Doppler Current Profiler (ADCP). Instruments used to collect temperature data include the SBE-37 MicroCAT, SBE-19 SeaCAT, Brancker Temperature Recorder, and Hugrun Seamon Mini Temperature Recorder.

Station	Latitude	Longitude	Duration of Record	Temporal Resolution	Elevation (above sea level)
John Wayne Airport	33° 40' 48"N	117° 51' 59"W	July - Oct 2001	Hourly	16.5 m (54.1 ft)
ASOS Station					
Long Beach Airport	33° 48' 42"N	118° 08' 47"W	July - Oct 2001	Hourly	9.4 m (30.8 ft)
ASOS Station					
M7	33° 34.593'N	118° 01.256'W	July - Oct 2001	Minute	4 m (12 ft)

Table 2. Wind data used in thesis research

The S4 Current Meter operates on the theory of Faraday's law of electromagnetic induction. It measures the voltage resulting from the product of the speed of the conductor (here water flow), the magnitude of the magnetic field, and the length of the conductor. The magnetic field is produced by a circular coil driven by an alternating current, and the conductor length is the distance between the sensing electrodes. The FSI 2D-ACM works on the principle of measuring and comparing acoustic phase shifts. The instrument has four "fingers", each of which contain two transceivers, creating four acoustic paths. Flow velocity is measured using the phase shift of the sound pulses along the direct acoustic paths, rather than the backscattered signal. The Aanderra DCS-3900 works on the principle of the Doppler shift. The sensor transmits an acoustic pulse into the water and measures the frequency shift of the return energy. The internal compass circuit then enables the DCS-3900 to determine the current speed and direction. The temperature is measured using a temperature dependent crystal-oscillator-circuit.

The RDI Workhorse ADCP also works on the principle of the Doppler shift. It transmits sound at a fixed frequency and listens to the sound backscattered from particles in the ocean. These particles may be plankton or sediment suspended in the water, and on average, move at the same horizontal velocity as the water. ADCPs measure current profiles, and break up the profiles into uniform parts called depth cells (commonly called bins). The ADCP measures average velocity over each depth range of the bins. In making a determination of the top "good" bin for each ADCP, criteria from the

Workhorse ADCP Technical Manual and the ADCP Practical Primer are used. The echo amplitude, or intensity, is a measure of the signal strength returned to the ADCP, and is related to the Automatic Gain Control (AGC) of the ADCP. As the sound travels further away from the transducer, the signal-to-noise ratio decreases, as does the echo intensity and the correlation values. For an upward looking ADCP, as is used for this study, as the surface is approached, the echo intensity will begin to increase. This is due to the much stronger return of sound from the sea surface than from scatterers in the water. Therefore, in making a determination of the top bin to use in analysis, the bin where the echo intensity and correlation increase sharply after a steady decrease should be used. M3 contains a 1200 kHz ADCP (bin length 1 m), M5 contains a 600 kHz ADCP (bin length 1 m), and M6 (bin length 2 m), M7 (bin length 2 m), M10 (bin length 2 m), and M11 (bin length 2 m) contain 300 kHz ADCPs.

The SBE-37 MicroCAT measures temperature by applying an alternating current to an airtight VISHAY reference resistor and an ultra-stable aged thermistor. The SBE-19 SeaCAT measures temperature using a Pyrex cell and pressure-protected thermistor. The Brancker temperature recorder measurements are made by comparing an airtight aged stable thermistor with an oil filled metrology standard fixed resistor. The Seamon mini temperature recorder employs a microprocessor-controlled temperature recorder. Each recorder is calibrated in a highly accurate and stable temperature bath, and the calibration coefficients are stored in its memory. All moorings, with the exception of 12, contain a SeaCAT, MicroCAT, or both. In addition, M5, M7, and M11 contain the Brancker temperature recorder, and M6, M9, M10, M12, and M13 contain the Hugrun mini temperature recorder.

2. Wind Data

Station 07 includes a meteorological station with a Handar sonic anemometer at an elevation of 4 m above the sea surface recording winds at a sampling rate of 1 minute. The data had periodic small gaps of 1 or 2 minutes, and was linearly interpolated onto a 1-minute time base. The Automated Station Observing System (ASOS) data from two airports, Long Beach (33^{o} 48' 42" N 118^{o} 08' 47" W) and John Wayne (33^{o} 40' 48" N 117^{o} 51' 59" W) consisted of hourly wind speed and direction. Long Beach Airport (LBH) is located approximately 30 km WNW of the HB study site and 4.5 km from the

coast. John Wayne Airport (JWA) is located approximately 9 km from the coast, behind Newport Bay. Hourly winds are computed based on the average wind speed and direction two minutes immediately preceding observation time. The elevation of the ASOS station at LBH is 9.4 m above sea level, while the elevation of the ASOS station at JWA is 16.5 m above sea level. The wind sensors consist of a rotating cup and vane whose electro-magnetic signals are converted into reportable values (ASOS User's Guide, 1998). The reported cutoff speed for ASOS is 2 knots, though the data here shows a cutoff speed of 3 knots (anything less than these speeds is recorded as 0 wind speed and 000 wind direction). ASOS stations also report variable winds, determined if the wind direction varies by 60^{o} or more during the two-minute observation period (if wind direction is recorded as variable, the true wind speed will still be recorded in knots).

THIS PAGE INTENTIONALLY LEFT BLANK

III. METHODS OF DATA ANALYSIS

A. INITIAL PROCESSING

The ocean temperature and currents, and wind data collected for Phase III of the HB investigation are broken into different files with different levels of processing and clean up. For this study, both the processed_raw and processed_ 3-hour low pass (3hlp) data are used in the various analyses, once determined that the results for the diurnal periods are not significantly different. The 40-hour low passed data are used to examine the low-frequency variability across the shelf. For some spectral analyses, the entire time series are used, which varied slightly in length, but again, did not create significantly different results. The processed_raw data have had minimal clean up and are at the original instrument time step. The processed_3hlp data have had a higher level of clean up performed by SAIC. Additionally, these data are filtered and decimated to 1-hour time intervals by SAIC. The 3-HLP filter applied to the data uses a Lanzcos kernel with half power point at three hours and greater than 95% suppression at periods less than one hour. It removes eight hours from the ends of the original time series. Some records that consisted of two or more deployments have been concatenated into one continuous time series. The maximum gap in the original data is approximately two days. An effort has been made to keep the data inserted into the 3-hlp files spectrally consistent and vertically coherent. The 40hlp data contain the 3hlp files which are further filtered with the 40-HLP Lanzcos kernel and subsampled to 6 hourly.

The wind data from the ASOS stations is also 3-HLP filtered and decimated to 1-hour time intervals. Winds reported as variable are replaced with a null value and are then filled and interpolated. There is also some question as to the accuracy of the orientation of the principal axes and diurnal ellipses for LBH and JWA, as well as the mean speed and direction. Due to the stall speed of 3 knots, and the recording of variable wind direction as well as a direction of 000 with speeds lower than 3 knots, the mean wind speed may be estimated slightly below the true mean, and the wind direction may have a more northerly component than it actually does.

A set of MATLAB programs called CMGTool (Coastal Marine and Geology), developed by USGS, loads netCDF files (which is the format of all the data files) and performs a number of different analyses on them. In addition, the program also produces graphs of the time series, computes different parameters such as wind speed and direction from u and v components, wind stress from speed and direction, and allows computed variables such as wind speed and wind stress to be saved and loaded into Matlab for further analysis. It can also be used to perform tidal analyses on scalar variables, such as sea level. A number of different functions in the program are used to analyze the temperature, ocean current and wind data from the moorings and the ASOS stations.

Coastline orientation for the HB study site is 306^o-126^o. This is used in determining alongshore and cross-shore winds for M7 and John Wayne Airport. Coastline orientation for Long Beach Airport is not as easily determined due to the inshore bend of the San Pedro Bay, but 270^o-090^o is used as the best estimate. The alongshelf direction for M10, M11, and M12 is 287^o, and 302^o for the remaining moorings. To ensure notation is clear, u is used for the east/west velocity components, v is used for the north/south velocity components, u_r is used for the cross-shelf direction, and v_r is used as the alongshelf direction. The usual oceanographic convention is used when discussing ocean currents as the direction toward which they are flowing, and the usual meteorological convention is used when discussing wind as the direction from which it is blowing.

B. PRINCIPAL AXES ANALYSIS

CMGtool is used to determine the mean speed and direction, and principal axes of the wind and ocean currents. Principal axes analysis is useful in that it gives a statistical picture of variance for a set of vector time series. The majority of variance, or maximum amount of data "scatter" is associated with the major axis, and the remaining variance, or minimum amount of data "scatter" is associated with the minor axis. The principal axes are defined in such a way that the velocity components along the principal axes are uncorrelated. The analysis consists of finding the maximum variance in observed velocity fluctuations $U'(t) = [u'(t), v'(t)]$ along the principal axes for a given location, where $u'(t)$ and $v'(t)$ are the east-west and north-south components of the wind or current

velocity, respectively. They are obtained from removing the means $\bar{u}$ and $\bar{v}$ from each point in the time series; i.e. $u'(t) = u(t) - \bar{u}, v'(t) = v(t) - \bar{v}$ (Emery and Thomson, 1997). Principal axes analysis is performed on all top ADCP bins and the shallowest current meters of the moorings, as well as the remaining bins on M5, wind data at M7, the ASOS data for both airports, and the wind stress at M7. In coastal or shallow areas, mean currents generally flow parallel to the coastline or local bottom topography. Therefore, the major axis usually parallels the orientation of the coastline and can be used to define the alongshore direction. For this study, both the processed_raw and 3hlp files are used for the principal axes analysis. This method includes all frequency information, and the principal axes may be used for a direct comparison with the diurnal ellipses.

C. SPECTRAL ANALYSIS

Spectral analysis is used to determine how the variance of a time series is distributed over frequency. Rotary, kinetic energy, coherence and phase, and auto spectral analysis were performed on the data. All analyses are performed using Matlab programs, which ingest the files and output the spectral coefficients. The programs are based on the discrete Fourier transform and the periodogram method. A Hanning window is applied with a 50% overlap to ensure correct confidence levels. As is usual practice, the mean and trend of the time series were removed before analysis. The program was run on both the processed _raw (in the original time step) and the 3hlp files, in order to ensure the spectral coefficients at periods greater than three hours did not change appreciably. The analyses are done by breaking up the record into integral multiples of 24 hours, in order to get an estimate exactly at the diurnal frequency, regardless of which file is used. For example, in the processed_3hlp files, the number of points per section used was 720 (30 days x 24 hours/day), and the sample interval was 1 hour. In the processed_raw files, the number of points per section for the 3-minute data was 14400 [(30 days x (24 hours/1day) x (60 minutes/1 hour))/3 minutes], and the sample interval was 0.05 hours. The number of points per section for the 1-minute data was 43200 (14400 points x 3), and the sample interval was 0.01666667 hours. The confidence interval for all spectra is 95%.

1. Kinetic Energy Spectra

The time series data collected in this study is a mixture of deterministic and stochastic processes. Deterministic processes, such as tides, are predictable, while stochastic processes, such as internal waves, are random. The frequency content of a long time series can be severely distorted when looking at only a small portion of it. Viewing only a small portion may actually act like a "window", and spectral energy can be leaked from the central frequency to nearby frequencies (Emery and Thomson, 1997). An important question when analyzing data is "What constitutes an independent sample?" A guide suggested by Emery and Thomson (1997) is that a highly correlated group of measurements is dependent, and at the same time, a group of measurements totally uncorrelated must be independent. In the case of uncorrelated data, the total number of measurements defines the number of "degrees of freedom". For the kinetic energy spectra, the degrees of freedom are increased using the aforementioned Hanning window, which resulted in approximately seven "pieces" of record for most of the analyses on the moorings. The u and v time series for the top ADCP bin or the shallowest current meter at each mooring are used for the kinetic energy spectra. The percent variance in the diurnal band is also calculated for all top ADCP bins and the shallowest current meters on all of the moorings, and for all ADCP bins on M5. This is accomplished by adding the kinetic energy spectral density for all frequencies at each mooring, dividing the density at the diurnal frequency by this total, and multiplying by 100 to obtain the percent.

2. Rotary Spectra

Rotary spectra separate the velocity vector of a certain frequency, ω, into clockwise and counterclockwise rotating circular components. The vector addition of these two components, rotating in opposite directions, causes the tip of the combined vector to trace out an ellipse determined by the relative amplitudes of the components. If one of the two components is zero, motion is circularly polarized, and if the two components have the same magnitude, motion is rectilinear. In many cases, the clockwise component is dominant in the northern hemisphere and the counterclockwise component is dominant in the southern hemisphere.

The rotary spectra program outputs the clockwise (+) and counterclockwise (-) spectral coefficients, as well as the rotary coefficient, semi-major and semi-minor axes, and the orientation, which is measured counterclockwise from east. The rotary coefficient is a useful property in that its magnitude is a quantitative measure of the eccentricity of the flow and its sign is a measure of the polarity of the flow. It has no units and ranges from r = +1 for clockwise motions, to r = 0 for unidirectional flow, to r = -1 for counterclockwise motions. These coefficients change a great deal with depth, time, and position. The output at the diurnal frequency is then used to create diurnal ellipses to compare with the results from the principal axes analysis.

3. Coherence and Phase Spectra

Coherence and phase spectra are calculated between all moorings and the wind at M7, and the two airport winds and the wind at M7. The times series of the top ADCP bins or shallowest current meters for all moorings and the wind records from the airports are truncated to the common time period, July 1, 2001 through October 12, 2001. They are each rotated into their respective diurnal ellipse orientations, obtained from the rotary spectra output, in order to ensure that the direction of maximum diurnal variability is used. The M7 wind record is input as the first time series, and the subsequent current meter moorings and airport wind records are input as the second time series. The two signals are perfectly coherent and in phase if the coherence is equal to one and the phase lag between the two signals is zero. If the two signals are completely unrelated the coherence will be zero. If the coherence lies somewhere between 0 and 1, then it may be assumed that some random noise is present in the signals, or the system relating the two signals is not linear. Though two records may be highly coherent, this does not imply a direct cause-and-effect association between the two time series. The phase output from the coherence and phase spectra program is first divided by 360^{o} and then multiplied by twenty-four hours in order to obtain the time lag between the currents and wind at each mooring.

D. WAVELET ANALYSIS

Wavelet analysis involves transforming a time series into a series of coefficients that contain all the information of the original signal, and in this sense is analogous to

Fourier analysis. In Fourier analysis, a signal may be reconstructed by adding sines and cosines of different periods together; in wavelet analysis, it may be reconstructed by adding wavelets of different scales and at different translations together. The wavelet scale is analogous to the period in Fourier analysis. The technique for both is the same: a convolution in which the signal and the analyzing function are multiplied together, and the integral of the product is computed (Hubbard, 1996). Continuous wavelet analysis actually involves a transform from the one-dimensional time series to a two-dimensional time frequency image. In performing the analysis, both the dominant modes of variability and their variations in time may be determined.

The method used for the wavelet analysis in this study is adapted from a guide written by Torrence and Compo (1998). "Wavelet function" is used to describe either orthogonal or nonorthogonal wavelets. The discrete wavelet transform is used with an orthogonal wavelet function, and a nonorthogonal wavelet function is used with either the discrete or continuous wavelet transform (CWT). The difference between the discrete and continuous wavelet transform lies in the choice of scales. In the continuous wavelet transform, an arbitrary set of scales may be used, while in the discrete wavelet transform, the set of scales is more limited. For this analysis the nonorthogonal wavelet function is used with continuous wavelet transform. The nonorthogonal analysis is redundant at large scales, creating a highly correlated wavelet spectrum at adjacent times. This also makes nonorthogonal transform useful in time series analysis because continuous, as opposed to step-like, variations in amplitude are expected.

The wavelet function used in this analysis is the Morlet wavelet, which is a product of a complex exponential plane wave and a Gaussian envelope (Figure 5):

$$\Psi_o(\eta) = \pi^{-1/4} e^{i\omega_o \eta} e^{-\eta^2/2}, \qquad (3)$$

where η is the nondimensional "time" parameter and ω_o is the nondimensional frequency. Using this as the wavelet function, a picture is constructed showing how the amplitude of the features of the signal changes in time, by changing the scale and translating in time. The wavelet function at each scale *s* is also normalized to have unit

energy, which ensures the wavelet transforms at each scale are directly comparable to each other. This is accomplished using:

$$\Psi\left[\frac{(n'-n)\delta t}{s}\right] = \left(\frac{\delta t}{s}\right)^{1/2} \Psi_o\left[\frac{(n'-n)\delta t}{s}\right], \tag{4}$$

where s is the wavelet scale and n is the translation parameter. The factor of $s^{-1/2}$ indicates $\Psi_o(\eta)$ is normalized.

In this analysis, the amplitudes of the wavelets are scaled by a unit amplitude sine wave, in order to ensure the amplitudes among different frequencies may be directly compared. Due to the width of the wavelet filter in Fourier space, a signal with sine waves of the same amplitude but different frequency will be "biased" toward one of the frequencies. The width of the wavelet function is defined as the e-folding time of the wavelet amplitude. At small wavelet scales, which resolve high frequency components, the wavelet itself is broad in frequency and the amplitude of the peaks in the spectrum is smoothed out. At large wavelet scales, which resolve low frequency components, the wavelet itself is narrow in frequency and the amplitude of the peaks in the spectrum is larger. A unit amplitude sine wave is fed into the program, and results in a unit amplitude response in the continuous wavelet transform. The continuous wavelet transform is then performed on a time series, and the results are divided by the scale factor appropriate for each period, based on the response of the unit amplitude sine wave.

The Morlet wavelet is both complex and contains many oscillations, therefore the wavelet combines both positive and negative peaks into a broad single peak. This analysis uses only the magnitude of the Morlet wavelet, as the phase information is not easily interpreted. The oscillatory nature of the Morlet wavelet makes it useful in capturing oscillatory behaviors in motions such as fluctuating wind and ocean currents. The ultimate goal of the CWT is to determine how the amplitude of the signal at a number of discrete frequencies, specifically diurnal and semi-diurnal for this study, changes with time.

In order to obtain an idea of the diurnal and semi-diurnal amplitude of the wind, ocean currents and isotherms, the continuous wavelet transform is performed on various

time series. These include the top ADCP bins of M3, 5, 6, and 7 in the along-ellipse direction, as well as the kinetic energy for the top, middle, and bottom of the water column for these moorings, and various ADCP and current meters across the shelf. It is also performed on the three wind records and various temperature records and isotherm displacements.

E. LINEAR CORRELATION

The linear correlation coefficient, *r*, is calculated between the diurnal period wavelet amplitude of the wind at M7 and the surface currents of the moorings. The correlation coefficient is calculated to determine if the variations in the diurnal period wavelet amplitudes of the wind at M7 are correlated with the diurnal period wavelet amplitudes of the near-surface currents. The correlation coefficient is a dimensionless quantity whose value lies between –1 and +1 (0 is no correlation and +/- 1 is maximum correlation). The degrees of freedom used to estimate the significance level is the number of total hours in the record divided by 24 hours. The estimate uses 24 hours assuming an independent estimate of the wind on a diurnal basis.

IV. RESULTS

A. WINDS AND NEAR-SURFACE CURRENTS

1. Ocean Currents

Highly energetic diurnal surface currents dominate the San Pedro Shelf from July 1 through October 12, 2001. The diurnal currents dominate the semi-diurnal currents in the upper water column. The dominance of diurnal energy at the surface is evident in the kinetic energy spectra for the top ADCP bins of M5, M6, and M7 (Figure 6). In contrast, the semi-diurnal kinetic energy at M5 is slightly larger than the diurnal kinetic energy at a depth of 21.92 m, only 3 m above the bottom (Figure 7).

Another comparison between the diurnal and semi-diurnal currents is seen in the difference in sizes of the near-surface current ellipses, created from the output of the rotary spectra (Figure 8). The diurnal ellipses are much larger than the semi-diurnal ellipses. The former are all oriented close to the large-scale alongshore direction, with the exception of M7, which has a slightly cross-shore orientation. The reason for the anomaly at M7 is unknown, but the orientation of the ellipse is believed to play a role in some of the differences seen in the subsequent analyses. The phase of the diurnal ellipses is nearly uniform across the array.

The semi-diurnal ellipses are much narrower than the diurnal ellipses, and in the case of M3, M5, M9, M10, and M13 are nearly rectilinear. Traveling from the coastal region outward toward the shelf, both the diurnal and semi-diurnal surface ellipses become more circular, and all are clockwise polarized.

Principal axes ellipses and diurnal ellipses are compared to give an idea of the magnitude of the diurnal currents. The mean speed of the ocean currents increases moving offshore from M3 to M6, and then there is a slight decrease in speed at M7 (Figure 9). M10 and M11 share very similar magnitude means to that of M5, while M12 has the greatest mean speed at 20.5 cm/s and M13 has the smallest mean speed at 3.3 cm/s. All of the means are oriented close to the alongshore direction (Table 3), as are the major axes of the diurnal and principal axes ellipses, which indicates the majority of the variance is in the alongshore direction. Except for M13, where the mean is smaller than

the semi-major principal axis, the mean speeds everywhere on the shelf are the larger than the semi-major principal axis and oriented southeastward. This is typical of the San Pedro Shelf during the summer, as pointed out in Winant and Dorman (1997), when energetic and persistent currents dominate the region, and the means are larger than the fluctuations.

Mooring/Station	Mean Speed	Mean Direction	Semi-Major Axis	Semi-Minor Axis
M3	8.99	124.2	6.97	2.78
M5	15.4	124.5	8.14	4.2
M6	19.69	122.8	9.05	5.11
M7	17.17	133.7	7.75	4.95
M9	10.29	118	7.01	2.69
M10	14.28	118.9	8.22	3.79
M11	14.88	128.3	8.39	4.3
M12	20.49	121.5	8.6	5.83
M13	3.31	135.3	6.2	3.36
M7 Wind	2.4	091	1.55	0.63
JWA	1.95	036	0.85	0.54
LBH	0.93	051	1.13	0.64
Note: Units are m/s for wind and cm/s for ocean currents				

Table 3. Mean speed and direction toward and principal axes of wind and ocean currents

Using the output from the kinetic energy spectra, the percentages of variance in the diurnal band of the top ADCP bins and surface current meters of the moorings are computed (Table 4). This is accomplished using the kinetic energy spectral estimate at 1/24 hour. In general, the diurnal variance accounts for a large portion of the total variance in the surface currents, and far exceeds the semi-diurnal variance. The percent variance in the diurnal band increases moving offshore from M3 to M6, with a slight decrease at M7, but the percent variance in the diurnal band over the outer shelf still accounts for almost one-fifth of the total variance. M12 and M6 have the first and second largest mean speeds, and have the first and second largest diurnal percent variance, with the diurnal variance at M12 accounting for almost 30% of the total. M13, which is closest to shore, has the smallest mean speed and the smallest percent diurnal variance.

Note that there is no inconsistency between the fact that the diurnal and principal axes ellipses are similar in size, while the diurnal variance accounts for only about one-fifth of the total variance, since the large scatter in the velocity shows the variance in the principal axes is only a fraction of the total variance (Figure 10).

Mooring	Bin #	Depth (m)	Diurnal %	Semi-Diurnal %
3	10	4.45	11.2261	3.8325
5	17	3.63	16.8177	2.0192
6	12	3	21.0768	2.2144
7	23	3.83	18.516	4.0567
9		5	11.4	2.5
10	14		13.7	2.2
11	22		10.5	2.4
12		1	29.8	1.5
13		5	8.7	1.7

Table 4. Percent variance in diurnal and semi-diurnal bands for all moorings

2. Wind

The wind at M7, the only over water study site, is used to compare with the amplitude and direction of the ocean currents. The diurnal signal dominates the record, but it varies in amplitude over the duration of the record (Figure 11). The wind speeds attain their largest magnitude between July 8 and July 13, with wind speeds in excess of 9 m/s at times during the day. Figure 12 shows the wind direction at M7 rotated into the coastline orientation of 306^{o}-126^{o}. A wind direction of 0^{o} corresponds to 306^{o}, or upcoast, while a wind direction of 180^{o} corresponds to the downcoast direction, 126^{o}. The predominance of downcoast winds is made clearer in a stick plot (Figure 13). The majority of the winds are northwesterly, in the same direction that the mean ocean currents are directed. There is an onshore component to the wind both when the winds blow upcoast and downcoast. A blow-up of the winds at M7 for two weeks in September gives a better indication of the clear diurnal fluctuation in the winds (Figure 14). The days on the x-axis begin at 0000 GMT, which corresponds to 1700 Pacific Daylight Savings Time (PDT). The onset of the sea breeze is approximately 1400 PDT, with a maximum occurring at 1600 PDT, and becomes increasingly alongshore into the afternoon and evening. Beardsley et al (1987) discuss a similar occurrence off northern California and attribute it to a modification of the southward flowing marine layer. This modification is brought on by a sharp eastward bend in the coast that causes the marine layer flow to thin and expand horizontally and accelerate. However, opposed to Huntington Beach, the winds off northern California have an extremely small cross-shore component. The onset of the land breeze occurs at approximately 0300 PDT, and is considerably weaker in magnitude than the afternoon sea breeze. This is consistent with

sea breeze theory. During the summer, maximum heating of land occurs in the afternoon, which coincides with the maximum pressure difference and strongest wind.

The mean speed of the wind is small, ranging from 2.4 m/s at M7, to 1.95 m/s at JWA, and 0.93 m/s at LBH, which is typical for the Southern California Bight during the summer. For M7 and JWA, the means are larger than the semi-major axis, and for LBH the mean speed (0.93 m/s) is very similar in magnitude to the semi-major axis (1.13 m/s). The magnitude of the mean wind at LBH is reduced due to the sheltering influence of the low coastal mountains to the north and south of the station. The orientation of the mean wind for M7 and LBH is slightly cross-shore (091^{o} and 051^{o}, respectively), while the orientation of the mean for JWA is entirely cross-shore (036^{o}).

The orientation of the principal axes and diurnal ellipses for the winds are more variable than for the currents (Figure 15). The principal axes ellipse at M7 is oriented alongshore in the same direction as the ocean current ellipses, while the diurnal ellipse has a slight cross-shore orientation (104^{o}). The orientation of the diurnal ellipse and the mean speed at M7 are very close, indicating the mean direction of the wind is most likely due to the diurnal sea breeze. The principal axes ellipse at LBH is oriented in the alongshore direction, and the diurnal ellipse is oriented more east-west, due to topographic steering by low coastal mountains to the north and south of the station. The principal axes ellipse for JWA is oriented in the cross-shore direction (039.4^{o}), as is the diurnal ellipse. The diurnal ellipse, however, is entirely collapsed and has no alongshore component, indicating the diurnal sea breeze at this station is entirely cross-shore.

The rotary spectral peaks for M7, JWA, and LBH fall on 24 and 12 hours (Figure 16). The diurnal energy is much larger than the semi-diurnal energy at M7 and JWA, but only slightly larger at LBH. In the diurnal band, clockwise energy is slightly larger than the counterclockwise energy at M7, and dominates over counterclockwise energy at LBH. In contrast, diurnal clockwise and counterclockwise energy are equal at JWA. The energy in the semi-diurnal band is slightly different. Clockwise energy is slightly larger than counterclockwise energy at M7 and LBH, and equal at JWA.

The output of the rotary spectra is used to show the comparative sizes of the semi-diurnal and diurnal ellipses (Figure 17). The diurnal ellipses, like those for the ocean

currents, are much larger than the semi-diurnal ellipses. The semi-diurnal wind ellipses are oriented alongshore for LBH and M7, and cross-shore for JWA, very similar to the principal axes ellipses. The semi-diurnal ellipses are also narrower than the diurnal ellipses at all stations, and in the case of JWA, both the semi-diurnal and diurnal ellipses are rectilinear. The diurnal band includes 20 to 33% of the variance in the wind records (Table 5).

Station	Diurnal %	Semi-Diurnal %
M7	20.6314	1.1486
LBH	20.4238	6.7334
JWA	32.897	1.6877

Table 5. Percent variance in diurnal band for meteorological stations

Wind stress at M7 is calculated using CMGTool, and principal axes and rotary spectra are computed. The Large and Pond (1981) formulation is used to adjust wind speeds from the sensor height to 10 m. Then the Wu (1980) formulation for the drag coefficient is used in the calculation of wind stress. The mean wind stress at M7 is very small, 0.023 N/m^2, and is oriented southeastward in essentially the same direction as the wind (099^o) (Figure 18). The diurnal wind stress ellipse is narrower than, and oriented in the same direction as the diurnal wind ellipse, indicating the diurnal wind stress is almost entirely alongshore.

3. Coherence Between Wind and Ocean Currents

The component of velocity parallel to the major axis of the near-surface diurnal ellipse is calculated for each of the moorings and wind records. Table 6 is the coherence and phase results at the diurnal and semi-diurnal frequencies for these along-ellipse components of velocity for all of the moorings across the shelf and the two airports. M7 wind leads the majority of the diurnal currents across the shelf, except M7 and M11, by 0 to 2 hours. The time lag between M11 and the wind at M7 is extremely small, but the currents at M7 lead the wind at M7 by 9 hours. The currents at M7, however, are clearly in-phase in the alongshore direction with the remaining moorings across the shelf (Figure 8). This large difference in time lag could be due to the slightly cross-shore orientation of the diurnal ellipse at M7. The wind at LBH is in phase with the wind at M7, however JWA leads the diurnal wind at M7 by 2.6 hours; when the wind is downcoast at M7 the wind is entirely onshore at JWA (Figure 17). This demonstrates the important difference

between the over-water wind and the slightly inland land-sea breeze system. The diurnal currents and wind are all very coherent, well above the 95% confidence level.

The semi-diurnal current phases show a completely different nature than the diurnal current phases over the study site. The semi-diurnal ocean currents at the moorings lead the wind, with the exception of M7, with time lags of several hours. The coherence between the semi-diurnal wind and ocean currents is extremely small, with only the other wind records, JWA and LBH, being coherent with the M7 winds at the 95% confidence interval. While the diurnal winds and currents are nearly in phase, with flow everywhere in the same direction within two hours of one another, the phase of the semi-diurnal wind and currents varies widely across the shelf (Table 6).

M7/	Diurnal				Semi-Diurnal			
Mooring	M7/Moor leads	Phase (deg)	Time Lag (hr)	Coherence	M7/Moor leads	Phase (deg)	Time Lag (hr)	Coherence
M3	M7 leads	-24	-1.6	0.94	Moor leads	105	7.0	0.30
M5	M7 leads	-16	-1.1	0.97	Moor leads	71	4.7	0.24
M6	M7 leads	-18	-1.2	0.98	Moor leads	101	6.8	0.12
M7	Moor leads	136	9.1	0.95	M7 leads	-153	-10.2	0.21
M9	M7 leads	-10	-0.7	0.93	Moor leads	104	6.9	0.25
M10	M7 leads	-3	-0.2	0.97	Moor leads	89	5.9	0.07
M11	Moor leads	2	0.1	0.96	Moor leads	58	3.8	0.09
M12	M7 leads	-28	-1.9	0.98	Moor leads	51	3.4	0.32
M13	M7 leads	-8	-0.5	0.94	Moor leads	127	8.4	0.40
JWA	JWA leads	39	2.6	0.96	JWA leads	99	6.6	0.80
LBH	M7leads	-4	-0.2	0.99	M7 leads	-13	-0.8	0.94
Note: 95% confidence level for coherence is 0.726								

Table 6. Coherence/phase between M7 winds and moored currents/airport winds

B. VERTICAL VARIATION OF CURRENTS

The mean speed of the currents at M5 decreases from 15.4 cm/s at a depth of 6 m to 2.3 cm/s at a depth of 22. The orientation of the mean rotates counterclockwise from 124.5^{o} at the surface to 116.5^{o} at a depth of 15 m, then rotate counterclockwise to 147.2^{o} at the bottom (Table 7). The means turn slightly toward shore in the upper water column, and then turn increasingly offshore at depth. The orientation of the semi-major axes of the principal axes ellipses for M5 rotate clockwise from the surface to the bottom. The magnitude of the mean speed above 17 m is larger than the semi-major axis, and below this depth the means are smaller than the semi-major axis. The mean speeds become

progressively smaller than the semi-major axis traveling downward in the water column because the currents are surface intensified.

Depth (m)	Mean Speed(cm/s)	Orientation
5.92	15.4	124.5
6.92	14.8	123.8
7.92	14.2	123.1
8.92	13.5	122.2
9.92	12.8	121.2
10.92	12	120
11.92	11.2	118.8
12.92	10.4	117.6
13.92	9.6	116.7
14.92	8.7	116.5
15.92	7.8	116.9
16.92	6.9	118.2
17.92	5.8	120.3
18.92	4.8	123.3
19.92	3.8	127.5
20.92	2.9	134.8
21.92	2.3	147.2

Table 7. Mean speed and orientation of ocean currents for M5.

While the upper water column is dominated by diurnal energy, the lower water column is dominated by semi-diurnal energy. This is evident in the rotary spectra for various moorings along the shelf. A representative example is the rotary spectra at the surface and bottom of the water column at M3 (Figure 19). Though the records are broken into integral multiples of 24 hours, the peak energy in the kinetic and rotary spectra in the ocean currents is seen at 24 hours (S1) and 12.413 hours, as opposed to exactly 12 hours. The energy at 12.413 hours is the closest spectral estimate to M2, which is 12.42 hours, indicating a large tidal signal present in the currents. The diurnal peak is larger than the semi-diurnal peak at a depth of 4 m, while the semi-diurnal becomes increasingly larger traveling down through the water column, and is larger than the diurnal peak at a depth of 13 m. Clockwise energy is dominant in both the diurnal and semi-diurnal peaks at both the surface and the bottom of the water column at M3.

The vertical structure of the diurnal and semi-diurnal energy at M3 is quite different (Figure 20). While the energy reaches a minimum in the middle of the water column in both frequency bands, at approximately 8 m for the diurnal frequency and 7 m for the semi-diurnal frequency, the diurnal energy is much more surface intensified. In

the upper several meters of the water column, the diurnal and semi-diurnal energy differ markedly. At the diurnal frequency, the clockwise energy increases dramatically from 8 m to the surface, with a final value of approximately 14500 (cm^2/s^2)/cph. The counterclockwise energy, however, increases only slightly over the same range, and has a near-surface value of approximately 3500 (cm^2/s^2)/cph. At the semi-diurnal frequency, both the clockwise and counterclockwise energy do not change appreciably in the upper several meters of the water column. The difference in the uppermost values of energy, 2700 (cm^2/s^2)/cph for the counterclockwise energy and 3400 (cm^2/s^2)/cph for the clockwise energy, is also not nearly as great as the difference for the diurnal values. The large increase in spectral energy in the upper water column at the diurnal frequency is indicative of a wind-driven influence.

Below approximately 8 m, the energy in both the semi-diurnal and diurnal band begins to increase. The energy in the semi-diurnal band is larger than the energy in the diurnal band, and clockwise energy continues to dominate. In comparing the near-bottom values, the clockwise energy in the semi-diurnal band is much larger than the counterclockwise energy, while the clockwise energy is only slightly larger in the diurnal band. The spectral energy reaches a near-bottom maximum of approximately 9500 (cm^2/s^2)/cph for the semi-diurnal frequency, and approximately 5400 (cm^2/s^2)/cph for the diurnal frequency.

Figure 21 shows the variation of the rotary coefficient with depth at M3 for the diurnal and semi-diurnal frequencies. The diurnal and semi-diurnal currents are clockwise at the surface. The rotation of the diurnal currents is strongly clockwise (0.6 rotary coefficient), while the rotation of the semi-diurnal currents is nearly rectilinear (0.1 rotary coefficient). Traveling down in the water column, the rotation of the diurnal currents changes to rectilinear and slightly counterclockwise (0 and –0.1 rotary coefficient) in the mid-water column, to clockwise near the bottom. The rotary coefficient of the semi-diurnal currents remains clockwise and increases steadily with depth, becoming more circular.

The rotary coefficients at M5 are very similar to those at M3. At both locations, the coefficients reach a minimum in the mid-water column, but those at M5 remain

clockwise throughout the entire water column. The rotary coefficients are related to ellipses in that they describe their direction of rotation and eccentricity. Figure 22 shows how the diurnal ellipses vary with depth at M5. The diurnal ellipses rotate clockwise and decrease in magnitude with depth, becoming rectilinear in the alongshore direction at a depth of 12 m. From the surface to 13 m, the ellipses are also oriented in the alongshore direction. The ellipse at a depth of 14 m is oriented in the cross-shore direction and is the smallest in magnitude. The remaining ellipses rotate clockwise, increase in magnitude, and become more circular. This suggests the depth of the wind-driven influence on the currents may be about 13 m.

The variation with depth of the percent variance in the diurnal and semi-diurnal bands at M5 is notable in that at the surface the diurnal band accounts for much more of the variance than the semi-diurnal band (Table 8). The variance contained in the diurnal band decreases with depth until 13 m where it reaches a minimum value of 2.3%. Below this depth the percentage begins to increase and reaches a value of approximately half the surface value near the bottom. The percentage of variance in the semi-diurnal band, however, has quite a different vertical profile. It increases steadily from the surface to the bottom, where it accounts for 12.9% of the energy. As the tidal energy along the West Coast is predominantly semi-diurnal, a large amount of energy is expected at the semi-diurnal frequency, which is seen in the lower water column. The large amount of diurnal energy in the upper water column must have a source different from the barotropic tide, which is presumably the input of the sea breeze.

Bin #	Depth (m)	Diurnal %	Semi-Diurnal %
17	5.92	16.82	2.02
16	6.92	14.00	2.40
15	7.92	11.14	2.78
14	8.92	8.42	3.21
13	9.92	5.91	3.84
12	10.92	3.89	4.62
11	11.92	2.66	5.61
10	12.92	2.27	6.54
9	13.92	2.76	7.45
8	14.92	3.64	8.27
7	15.92	4.69	9.20
6	16.92	5.73	10.25
5	17.92	6.88	11.15
4	18.92	8.09	11.84
3	19.92	8.97	12.35
2	20.92	9.21	12.70
1	21.92	8.77	12.86

Table 8. Percent variance in diurnal and semi-diurnal bands for M5

C. TEMPORAL VARIABILITY OF THE DIURNAL WIND AND OCEAN CURRENTS

1. Ocean Currents

The amplitude of the diurnal signal in the upper ocean varies over the course of the summer. Continuous wavelet analysis is used to try to explore this variability qualitatively and quantitatively. The kinetic energy is examined for this purpose. By looking at kinetic energy rather than a single component of velocity, we avoid having to choose a component of velocity along a single direction, which might bias the results towards one frequency over another. Also, since kinetic energy is a function of the square of the velocity, the difference between the maxima and minima will be enhanced.

M6 lies in the middle of the HB study site and is used to compare with near-coast and down-coast moorings. The continuous wavelet transform of the kinetic energy of the near-surface currents shows two distinct bands of increased amplitude currents, the diurnal and semi-diurnal (Figure 23). The largest amplitude diurnal energy is present July 11-15, 23-27, and September 22-23. Smaller amplitude diurnal energy is also present August 17-27, September 8-9, 11-18, and October 7-12. Almost no diurnal energy is discernable August 1-18, August 27-September 7, and October 1-7. The largest values of semi-diurnal energy present near the surface (Figure 23a) occur at the same time as the largest values of diurnal energy, indicating there is not a shift between diurnal

and semi-diurnal energy over the course of the summer. While the semi-diurnal energy is always very weak when the diurnal energy is absent, the semi-diurnal energy is not always elevated when the diurnal energy is, such as August 17-22, and September 11-18.

Traveling down in the water column at M6 to a depth of 9 m, a few differences in the CWT are noted. While the pattern of increased amplitude diurnal and semi-diurnal energy is generally the same as the near-surface energy, there is a narrowing in time of the energy peaks (Figure 23b). The diurnal peaks near the surface, which span 4-10 days, do not span as long a time at 9 m. The amplitude of the diurnal and semi-diurnal energy is less than the near-surface energy (Note the difference in color bars for the different panels of Figure 23). There is also an increase in the amplitude of the semi-diurnal energy, and it is larger than the diurnal amplitude from July 24-25. Note also that the semi-diurnal energy appears to be less coupled to the diurnal energy in time than nearer to the surface. Semi-diurnal energy, which is present at all times the diurnal energy is present, is also present when diurnal energy is not present. This occurs on July 5-9, and August 1-2.

The final CWT examined for M6 is at a depth of 30 m, 5 m above the bottom. Again, the general pattern of energy remains the same with some slight differences in amplitude (Figure 23c). The peaks in diurnal energy remain narrower in time than the near-surface peaks. The amplitude of the diurnal energy is less than the energy seen at 9 m, with the exception of September 15-18, where the diurnal amplitude at 30 m is comparable to the diurnal amplitude at 9 m. The amplitude of the semi-diurnal energy, which at 9 m was comparable to the diurnal energy during two time periods, is comparable to (or greater than) the diurnal energy throughout the record at 30 m. The increased semi-diurnal energy present during July 5-9 at 9 m is not seen at 30 m, but semi-diurnal energy peaks are present at other times at depth when they are not seen higher in the water column (July 31-August 7, and September 3-4).

The pattern of temporal and vertical variations in diurnal and semi-diurnal energy at M6 is compared with that at M3, which is closer to the coast, and at M10, which is downcoast but on the same isobath as M6. The peaks in diurnal energy at M3 are smaller than the largest values at M6 at all depths. Near the surface, the maxima in semi-diurnal

energy at M3 are also smaller than further offshore, but the same is not true at depth. In comparing the near-surface continuous wavelet transforms, the diurnal peaks at M3 (Figure 24a) are weaker and more localized in time than the peaks at M10 (Figure 25a) or M6 (Figure 23a). Examples of this are the three distinct peaks of diurnal energy seen during July at M3, while only two peaks are seen at M10 and M6. While the largest amplitude diurnal peaks occur at the same time at all three locations, lower amplitude peaks occur at M3 which are not seen at M6 or M10.

The vertical variation of the diurnal and semi-diurnal energy at the three locations is also different. At M6, the diurnal and semi-diurnal energy generally occur at the same time throughout the water column, with two exceptions. At M3, the near bottom CWT shows a much greater amount of semi-diurnal energy present than diurnal energy (Figure 24c). The amplitude of the semi-diurnal energy present is either larger than or equal to the amplitude of the diurnal energy. M10 follows the same pattern as M6, where traveling down through the water column, the diurnal and semi-diurnal energy occur at the same time. However, the amplitude of the semi-diurnal energy at M6 is comparable to the diurnal energy traveling down through the water column, while the amplitude of the semi-diurnal energy at M10 is larger than the diurnal energy (Figure 25b). The amplitudes of the semi-diurnal energy in the near-bottom CWT at M10 are less than those found in the near-bottom CWT for M3 (Figure 25c). These results indicate that the amplitude of the semi-diurnal energy increases from the surface to the bottom of the water column, while the diurnal amplitudes decrease throughout the water column.

2. Wind

As previously mentioned, the winds over the HB study site are predominantly northwesterly with an onshore component (Figure 13). Although there is some variability in the amplitude of the diurnal signal in the wind, it is much more continuous than in the upper ocean currents throughout the three-month study (Figure 26). The largest diurnal amplitudes are seen July 7 – 14, August 10 – 18, and September 19 – 26. Smaller diurnal amplitude peaks are seen from July 18 – 27, the first week in August, and intermittently the first two weeks in September. The large amplitude diurnal energy corresponds to strong north-northwesterly winds, when a clear diurnal fluctuation is

present (Figure 13). Semi-diurnal energy occurs at the same time as the diurnal energy, though it is much reduced in amplitude.

While M7 represents the over-water site, the winds at JWA (Figure 26b) and LBH (Figure 26c) give an indication of winds over an extended area of the bight. The CWT for both locations shows almost continuous large amplitude diurnal energy. The peak amplitudes at each site are approximately equal in magnitude, and approximately half the amplitude of the diurnal energy at M7. While the large amplitude diurnal peaks in energy at LBH generally coincide with those at M7, those at JWA do not. At JWA, only one large amplitude peak is seen, August 26-31, and its value is larger than the maximum peaks at LBH. The majority of semi-diurnal energy seen at the airports occurs with the larger amplitude diurnal energy.

D. LOW FREQUENCY WIND AND OCEAN CURRENTS

1. Ocean Currents

The low-frequency flow over the HB study site in the summer of 2001 is contrary to the historical view presented in Hickey (1992) and Bray et al. (1999) of a maximum poleward flow in summer over the shelf regions of the bight. Measurements show that flow over the shelf is predominantly downcoast during the three-month study. The southeastward flow is typically faster than the northwestward flow, and downcoast velocity commonly exceeds 30 cm/s. Hamilton et al. (2001) also cite dominant downcoast surface flow over the shelf region in the summer of 1999, though it is reduced in magnitude compared to the summer of 2001. The low frequency flow plays a significant role in the diurnal variability of the shelf currents. A strong diurnal signal is seen when the direction of the low frequency currents is southeastward, and fades when the direction reverses to northwestward.

A comparison of the direction of the low frequency flow and the strength of the diurnal signal at M6 are shown in Figure 23b.[1] Large amplitude diurnal energy is present in the currents when the low frequency flow is southeastward, seen throughout July, the second half of August, and most of September. Diurnal energy is weak or absent when

[1] The data loss due to low pass filtering caused the start of the ADCP time series to be later than July 1, 2001. The low frequency currents at M6 are represented here by the velocity measured by an S4 current meter at 10 m depth. During the period of overlap, this time series is virtually identical to the time series measured at 9 m by the ADCP.

the low frequency currents are northwestward, seen during the first half of August, the first week in September, and the beginning of October. The southeastward currents reach their highest speeds in mid-July (Figure 27), which corresponds with the largest diurnal value in the CWT. The variability in the magnitude and direction of both the low frequency flow and higher frequency diurnal currents is seen in Figure 28. A strong diurnal fluctuation is clearly seen throughout July, but with the onset of current reversal to the northwest, the signal is lost and the currents are more disorganized. During periods of predominantly poleward flow, equatorward currents still occur intermittently, but during equatorward flow periods the direction never changes to poleward.

The relationship found between the low frequency currents and the large amplitude diurnal energy at M6 is also found at M3 (Figure 24a) and M10 (Figure 25a). At M3, more frequent current reversals occur over the three-month study than are seen at M6. The additional reversals at M3, seen in the beginning of July, August 21-22, September 5-6, and the beginning of October result in an absence of diurnal energy for these times.

The CWT at M13, which is on the same isobath as M3 and close to the head of the Newport Canyon, is markedly different from those at M3, M6, and M10 (Figure 29). Low frequency flow is also more prevalent at M13 than at the other sites. The only increased amplitude diurnal signals are seen in mid-July during steady equatorward flow, and intermittently throughout September, which coincides with the other diurnal energy seen across the shelf at this time. There is almost no diurnal energy present throughout all of August, when the mooring is dominated by variable flow. This relationship is made clearer in a plot of the magnitude and direction of the currents at M13 (Figure 30). As seen at M6, a clear diurnal fluctuation in the currents is present when the low frequency flow is strongly equatorward, and absent when the flow reverses direction.

2. Wind

Unlike the ocean currents, it is difficult to discern a prevalent shift in the direction of the low frequency wind for any period at M7 over the course of the summer. Several short 2-3 days reversals are seen, and one longer period reversal at the end of August (Figure 31). A blow up of this time reveals the clear diurnal fluctuations seen when the

wind is northerly (Figure 14) are not as strong when the wind is southerly (Figure 32). The smaller diurnal signal is also reflected in the CWT of the M7 wind, where during the last few days in August there is very little diurnal energy present (Figure 26a). The 2-3 day wind shifts correspond to lower amplitude energy in the CWT throughout the record, such as July 2-3, 15-16, August 19-20, and September 6-7 (Figure 26a). This is consistent with the theory presented in Beardsley et al. (1987) of a strong northerly coastal jet associated with alongshore diurnal wind fluctuations through the modification of the marine layer, in that when the low frequency wind shifts southerly, the dynamics of the jet breaks down and the diurnal motions are not as strong.

.

THIS PAGE INTENTIONALLY LEFT BLANK

V. DISCUSSION

A. DIURNAL AMPLITUDE OF WIND AND OCEAN CURRENTS

This study presents an integrated look at the response of the coastal ocean to diurnal wind forcing. Highly energetic diurnal currents dominate the Huntington Beach study site from July 1 – October 12, 2001. The clockwise energy of the diurnal currents, which dominates over the counterclockwise energy, is strongly surface intensified. Diurnal energy decreases rapidly from the surface to 10 m, supporting the notion of wind-driven diurnal currents. It reaches a minimum in the mid-water column, and increases slightly to the bottom (Figure 20).

The theory of frictional wind-driven ocean currents supports a steady decrease in energy with depth throughout the water column, so the increase in diurnal energy with depth after reaching a minimum in the mid-water column needs some explanation. Noble and Hamilton (2003) suggest a conceptual model for tidal period circulation over the shelf, which offers a possible explanation for the increase in diurnal energy below the wind-driven minimum (Figure 33). They describe a cross-shelf two-layer flow system, which consists of sea breeze forced flow in the upper several meters of the water column that is in phase with wind fluctuations, and 180^{o} out of phase with the subsurface flows between 10 and 20 m depth. They suggest that interactions with the sloping bottom give rise to vertical velocities. Alternatively, the differences in strength of the sea breeze forcing over the inner and outer shelf could result in diurnally alternating convergences and divergences which give rise to vertical velocities which deform the isopycnals and alter the pressure gradient forcing the flow at depth.

Noble and Hamilton (2003) find the temperature fluctuations in the upper layer are predominantly diurnal, and maximum amplitudes occur at depths that correspond to the minimum velocity. The CWT is performed on various temperature and isotherm displacement time series near the depth of the minimum diurnal period velocity in order to try to confirm the conceptual model. However, the temperature data was difficult to interpret and did not provide any definitive conclusions. Some of the difficulty results

from the fact that the isotherms intersect either the surface or the bottom sometime over the course of the record.

The diurnal current amplitudes also decrease near shore. Although this might be expected just due to the presence of the coastal boundary, it may also be related to the change in orientation of the diurnal wind ellipse from nearly alongshore over the outer shelf to cross-shore over land (Figure 17). Furthermore, poleward flow is more prevalent over the inner, relative to the outer, shelf and the results presented here indicate that diurnal current variability is reduced during times when the low frequency flow is poleward.

As is found off southern California (Lerczak et al, 2001), kinetic energy spectra of the ocean currents on the San Pedro Shelf are peaked at the diurnal frequency, 1 cpd, rather than the inertial frequency 1.107 cpd. The kinetic energy spectra of the wind at M7 have a narrow peak at the diurnal frequency as well, indicating a strong response of the ocean currents to the diurnal wind forcing. Inertial currents are often suppressed in the coastal ocean due to the coastal boundary.

The strength of the diurnal near-surface currents is also reflected in the size of the diurnal ellipses, as they are comparable in size to the principal axes ellipses, and much larger than the semi-diurnal ellipses, indicating that the diurnal variability constitutes a great deal of the variance at the surface. The diurnal variance decreases with depth, and eventually becomes less than the semi-diurnal variance. The alongshore currents are much stronger than the cross-shore currents in the nearshore. The mean flow, principal axes, and diurnal ellipses are all oriented close to the alongshore direction. The ellipses are also rectilinear near the coast and become increasingly circular offshore.

The CWTs for the wind and ocean currents show large amplitude diurnal energy present intermittently throughout the summer over the San Pedro shelf (Figures 23, 24, 25, and 26). The variability in the diurnal ocean current amplitudes is coherent from the surface to the bottom of the water column. The amplitude of the diurnal and semi-diurnal energy in the ocean is also correlated, as they are both present at the same time, with few exceptions. The variability of the diurnal near-surface currents does not appear to be

related just to the variability of the diurnal winds, as the diurnal winds are much more continuous over the course of the summer.

The inertial frequency for the Huntington Beach study site is 1.107 cpd, or a period of 21.68 hours. Since the diurnal frequency (1 cpd) is subinertial, freely propagating 24-hour period internal waves are not possible. However, as discussed in Lerczak et al. (2001), it is possible for the relative vorticity associated with the low frequency flow to alter the effective Coriolis parameter such that the diurnal frequency becomes super- rather than subinertial. It has been hypothesized that diurnal period ocean currents may be stronger during times when freely propagating internal waves at this period are possible.

Based on the discussion of the effect of low frequency flow and the generation of freely propagating internal waves in Lerczak at al. (2001), Hamilton (2003) defines periods for this data set when the effective local inertial frequency is lowered sufficiently to allow internal waves over the San Pedro Shelf. He determines that if the ratio of ζ/f is less than –0.18, then freely propagating internal waves are dynamically possible. He finds that over the inner shelf (M3), the criterion for internal waves is met very few times over the summer, while over the outer shelf (M6), the criterion is met throughout much of July and September (Figure 34). The CWT for the near-surface currents at M6 (Figure 23a) shows that the largest amplitude diurnal signals present in the record occur in July and the second half of September. The period of enhanced diurnal energy in August is of much lower magnitude than those in July and September.

Interestingly however, M3 shows the same temporal pattern of enhanced diurnal energy in the near-surface currents (Figure 24a) as is found at M6, even though the criterion for freely propagating internal waves is met only during three relatively brief time periods at this location. Furthermore, these three time periods coincide with the times when the low frequency flow is poleward, and the diurnal energy in the currents is greatly diminished.

During July and September, the enhanced diurnal energy near bottom is of greater magnitude at M6 than at M3 (Figures 23c and 24c, respectively), and the duration of the enhanced energy is of longer duration at M6 than at M3 at all depths, but it is unclear as

to whether this pattern may be attributed to internal waves or some other mechanism. The vertical structure of diurnal energy at M5 does not differ greatly between time periods when ζ/f is less than –0.18 over the outer shelf (meeting the criterion for freely propagating internal waves to exist), July 9-21, and times when the criterion is not met, August 9-21 (Figure 35). During July, there is more diurnal energy near surface, but the diurnal wind variability is also slightly greater during this time.

B. CORRELATION BETWEEN WIND AND OCEAN CURRENTS

The CWT analysis discussed to this point was performed on the time series of kinetic energy to avoid biasing the results towards one frequency or another by the choice of the scalar component of velocity. To perform the correlations of the amplitude variations of the diurnal period flow however, the component of flow (wind or current) in the direction of the orientation of the major axis of the diurnal ellipse was used. This ensures that the velocity component in the direction of maximum diurnal variability at each location is compared. The use of the kinetic energy vice the along-ellipse component of flow does not significantly change the temporal patterns, although naturally the difference between peaks and valleys is enhanced in the former since its based on the square of the velocity (compare Figures 23a and 36 and Figures 26a and 37).

The amplitudes of the diurnal period along-ellipse wind at M7 and the diurnal period along-ellipse ocean currents at M3, M5, M6 and M7 are highly correlated (Figure 38). Using 100 degrees of freedom, based on the number of hours over the whole record divided by 24 hours, the significance level for the 95% confidence interval is 0.195. The correlations of the diurnal amplitudes of wind and currents at zero time lag are all well above the 95% confidence interval. The maximum correlations occur on the order of one day lag time for all moorings. This indicates the diurnal near-surface currents are likely forced by the diurnal sea breeze.

The correlation between the low frequency alongshore current and the amplitude of the diurnal period along-ellipse velocity at M6 (Figure 36) is also computed. This correlation is also found to be significant, with a correlation coefficient of 0.34 at zero time lag. The location of the maximum correlation is on the order of two days. The

difference in time lags is thought to be a function of the scale of the Morlet wavelet, which is two days.

It bears reiterating that while the diurnal period currents are correlated with the low frequency currents and the diurnal period winds are correlated with the low frequency winds, the low frequency winds and currents are not correlated (Figures 13 and 28), as has been noted previously by Hamilton et al. (2001) and Hickey (1992, 2003). The diurnal period variability, which is predominantly in the alongshore winds, has been attributed to daily variations in the equatorward coastal jet in the atmosphere (Beardsley et al. 1987). Attempts were made to ascertain whether the diurnal variations in the predominantly alongshore ocean currents were similarly due to daily onshore-offshore movements or strengthening and weakening of the coastal upwelling jet, which would explain the significant lessening of diurnal period kinetic energy during times of poleward flow, but no definitive conclusion was reached.

THIS PAGE INTENTIONALLY LEFT BLANK

VI. CONCLUSIONS

Considerable wind and ocean data has been collected in conjunction with the Huntington Beach Phase III study. This provides an excellent opportunity to investigate the forcing mechanisms over a coastal shelf region. The diurnal sea breeze is a strong feature over the San Pedro Shelf, and contributes a large amount of energy to the near-surface currents. The low frequency background flow over the shelf plays an important role in how much energy the diurnal sea breeze can input into the ocean, but the dynamics of this are not fully explained in this study.

Upper ocean currents over the San Pedro Shelf show an energy peak at the diurnal frequency during the summer of 2001. These surface-intensified, clockwise-polarized currents decay with depth to a minimum at 10-13 m and increase in strength slightly below that. The diurnal currents also decrease in amplitude toward shore. The near-surface diurnal currents are in phase all across the shelf, and are close to being in phase with the M7 winds. There is 180^{o} phase shift in the diurnal currents with depth (Hamilton, 2003).

The amplitude of the diurnal energy of the ocean currents is correlated with the direction of the low frequency flow along the shelf, with large amplitude diurnal energy during times of equatorward flow, and little energy during times of poleward flow. The amplitudes of the diurnal currents along the direction of the major axes of the diurnal ellipses of wind and near-surface currents are also highly correlated. However, the low frequency currents and winds are not well correlated.

While the diurnal current amplitudes are surface-intensified, the semi-diurnal current amplitudes generally increase with depth, with the semi-diurnal energy exceeding the diurnal energy below about 8 meters over the inner shelf. The amplitude of the semi-diurnal energy is correlated in time with the diurnal energy, as it is enhanced when diurnal energy is enhanced, even though it may be very weak. Unlike the near-surface diurnal currents, the semi-diurnal currents are not in phase across the shelf. Another indication of the influence of the internal tides is the broadening of the semi-diurnal ellipses as the bottom is approached.

Although not presented here, it was determined that the presence of sewage contamination at Huntington Beach is not related to the diurnal circulation, nor for that matter, to any other coastal ocean transport mechanism (Noble et al., 2003).

A. NAVAL RELEVANCE

The study of the environment within the littoral area has taken on a much greater importance as the focus of the U.S. Navy has shifted from the open ocean, "Blue Water" warfare to sustaining operations from the littoral, or coastal oceans in recent years. The land sea breeze plays a critical role in understanding the governing motions within this area. Naval Amphibious Operations rely almost entirely on craft with limitations based on the condition of the coastal ocean. The Amphibious Assault is heavily dependent upon over-the-horizon movements, which take place entirely cross-shore. If certain environmental thresholds are exceeded, operations cannot proceed.

Many Special Warfare Operations also take place in coastal waters, and the delivery methods used in these operations are heavily dependent upon environmental conditions. Strong alongshore or cross-shore currents could hinder mission accomplishment, therefore the ability to predict the strength of these currents is very important.

Current operational ocean and atmospheric models predict wind strength and direction, as well as ocean currents, to a certain degree of accuracy. Therefore, understanding the response of the coastal ocean to the diurnal sea breeze is vital to making useful operational predictions to maximize the time and energy spent in planning, preparation, and execution of littoral operations.

B. RECOMMENDATIONS

The circulation over the San Pedro Shelf is influenced by a combination of forces, including diurnal wind forcing, tides, and low frequency background flow. The interaction of these forces is investigated here and some preliminary conclusions are drawn. However, more analysis is needed to understand the dynamics governing the results presented here. As this study is only one of a handful of investigations of the effect of diurnal wind forcing on near-surface ocean currents over the continental shelf, the data collected here provide an excellent opportunity to pursue these issues.

Further investigation and analysis, and comparison with numerical model results, could shed light on the small spatial scale variations in the sea breeze in this area.

THIS PAGE INTENTIONALLY LEFT BLANK

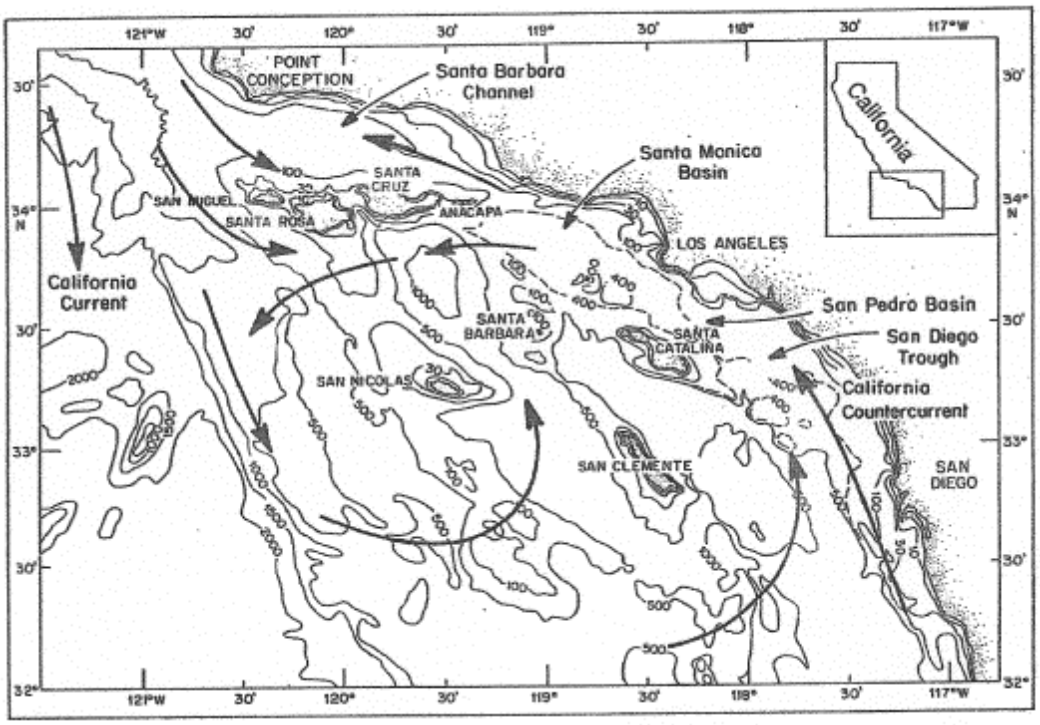

Figure 1. Mean circulation pattern and bottom topography in the Southern California Bight. Depth contours in fathoms (from Hickey, 1992).

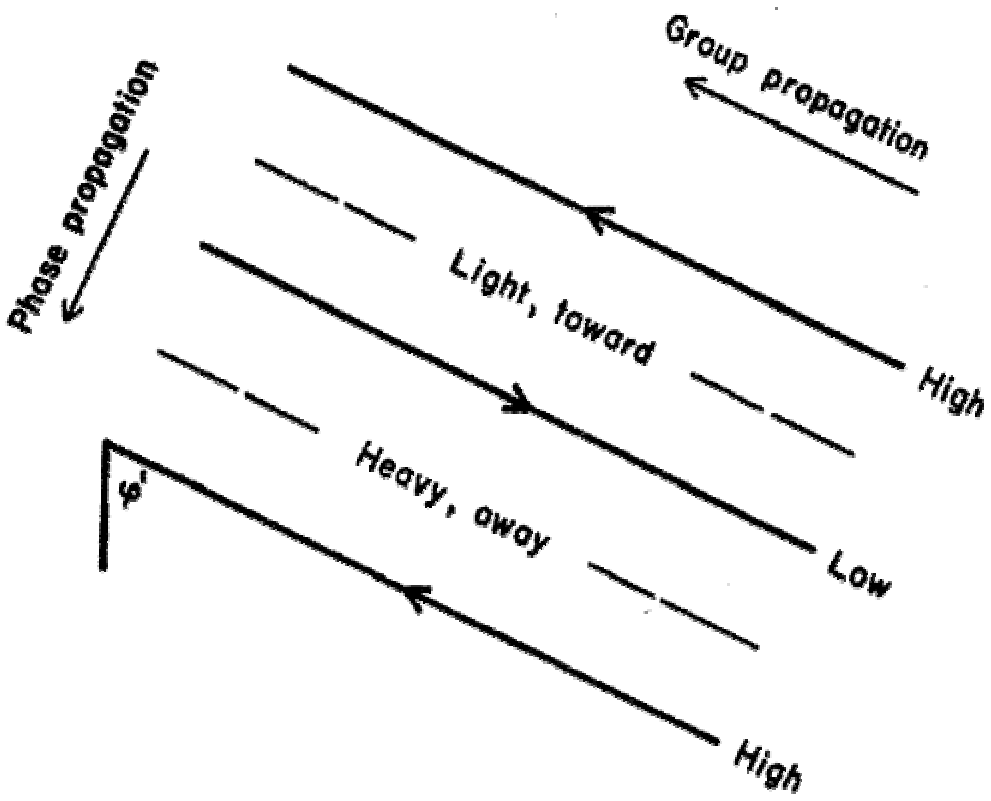

Figure 2. Relationship between direction of group propagation (C_g) and phase propagation, C_p (from Gill, 1982).

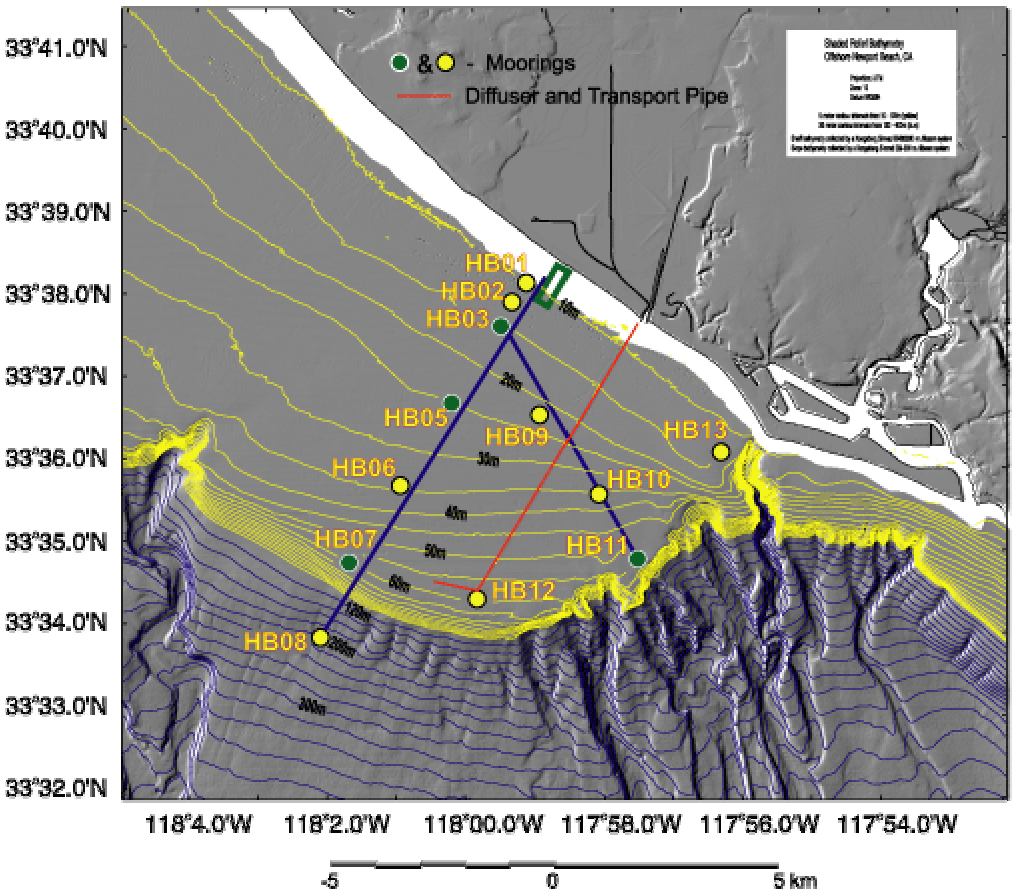

Figure 3. Location of moorings used in Huntington Beach Phase III Investigation. HB07 (also referred to as M7) is where meteorological measurements are taken. Yellow isobaths are at 10 m intervals, blue ones start at 120 m and are at 20 m intervals. (from Noble et al., 2003).

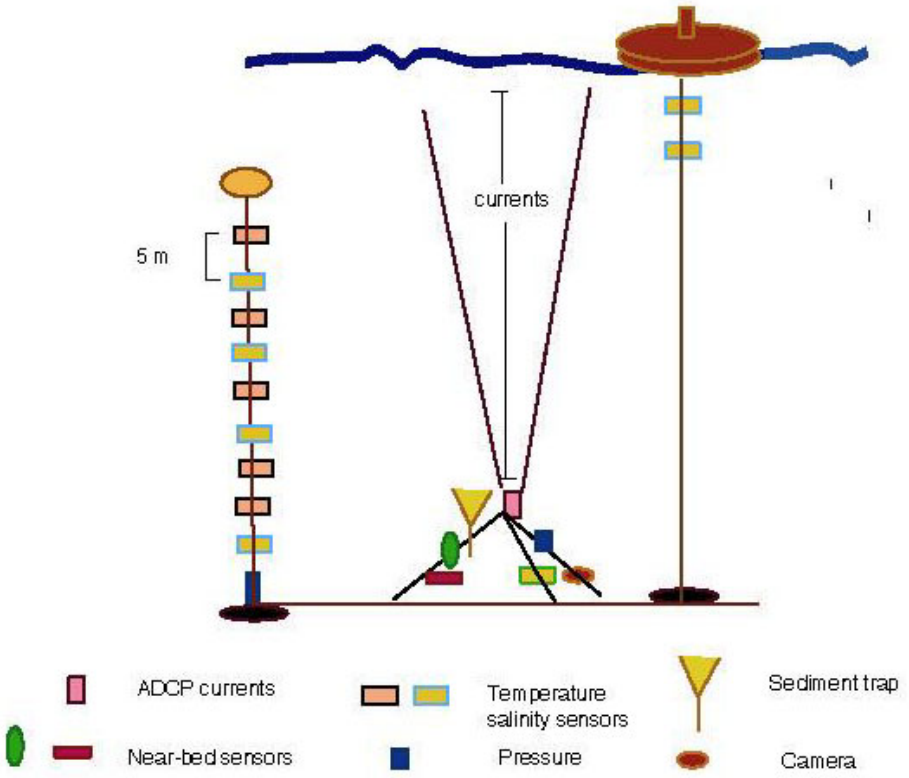

Figure 4. Typical set of instrumentation at a measurement site in the moored array over the San Pedro Shelf during Huntington Beach Phase III Investigation. Upward looking ADCP measures currents over the entire water column (from Jones et al., 2003).

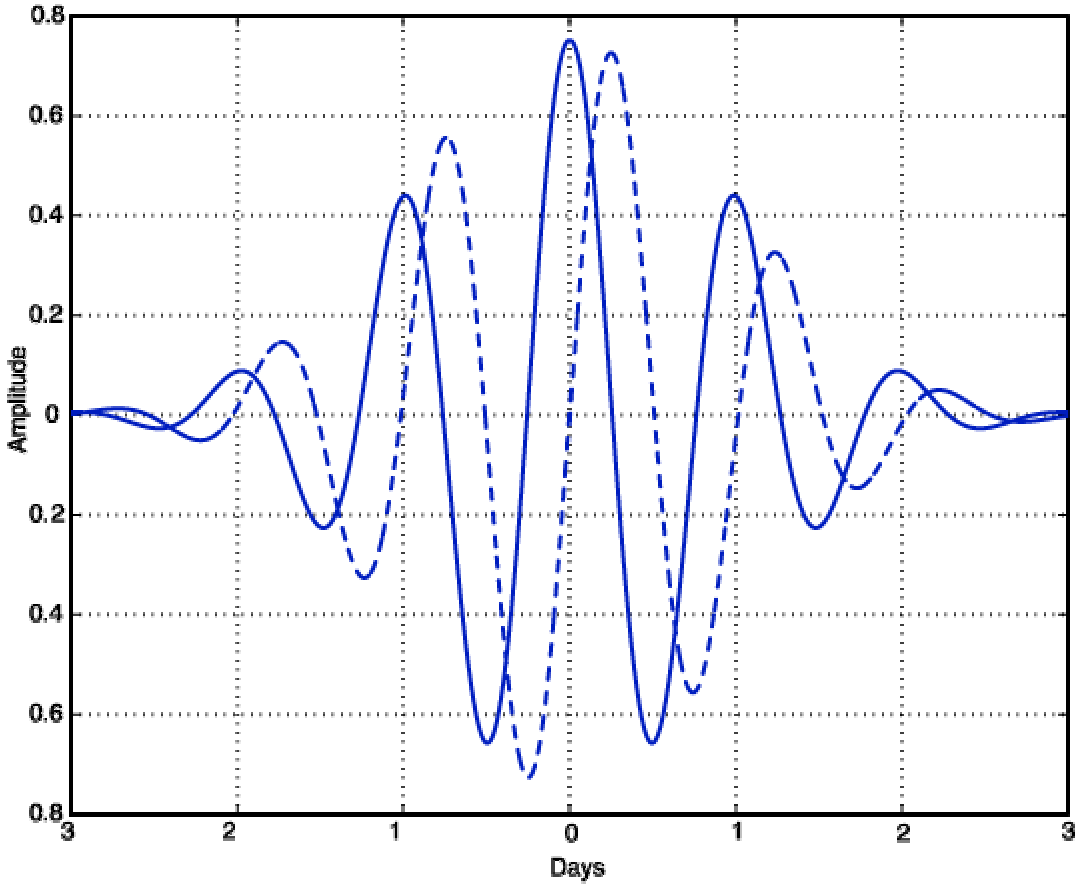

Figure 5. Morlet wavelet for Fourier scale of 24 hours. Solid line is real, dashed line is imaginary.

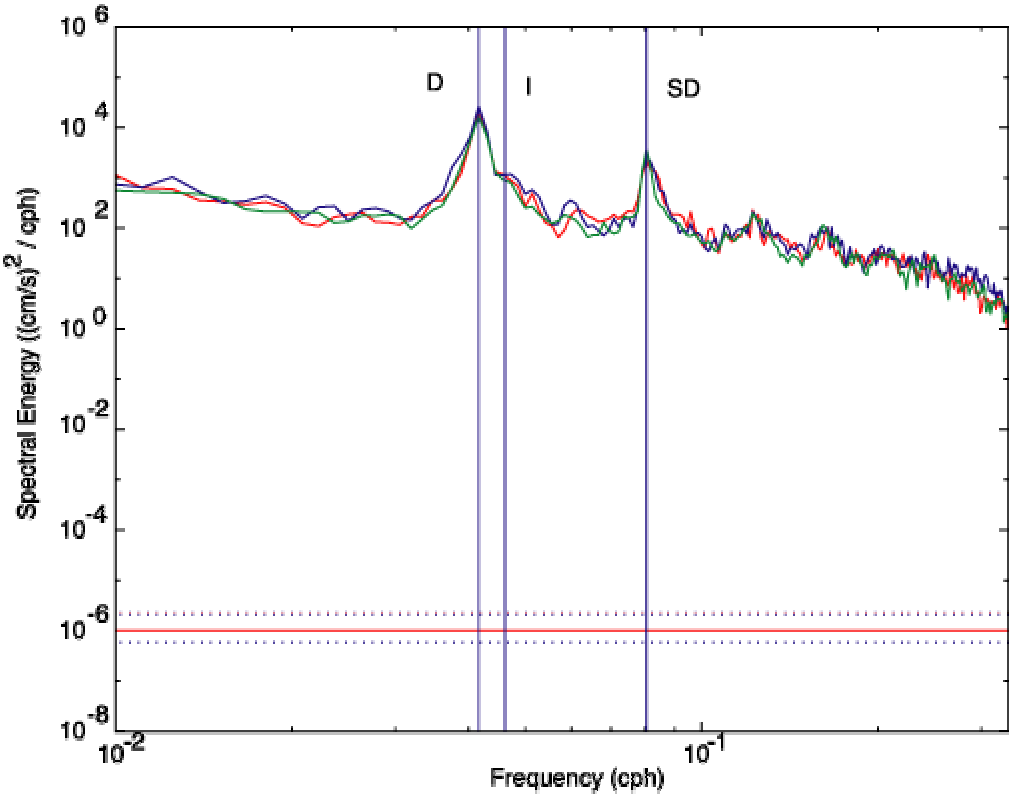

Figure 6. Kinetic energy spectra for near-surface currents (3 m to 7 m) at M5 (red), M6 (blue), and M7 (green). Diurnal, semi-diurnal, and inertial frequencies indicated by vertical blue lines. 95% confidence limits shown by horizontal solid red and dashed blue lines.

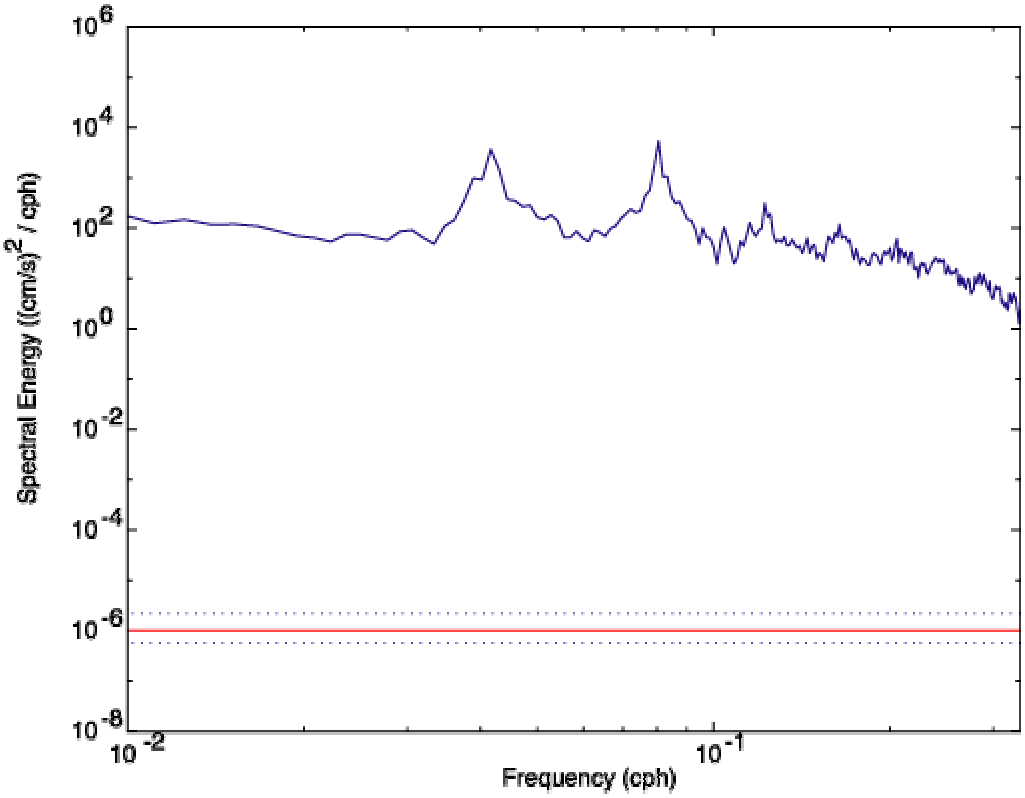

Figure 7. Kinetic energy spectra for M5 bin 1 (depth 22 m). 95% confidence limits shown by solid red and dashed blue lines.

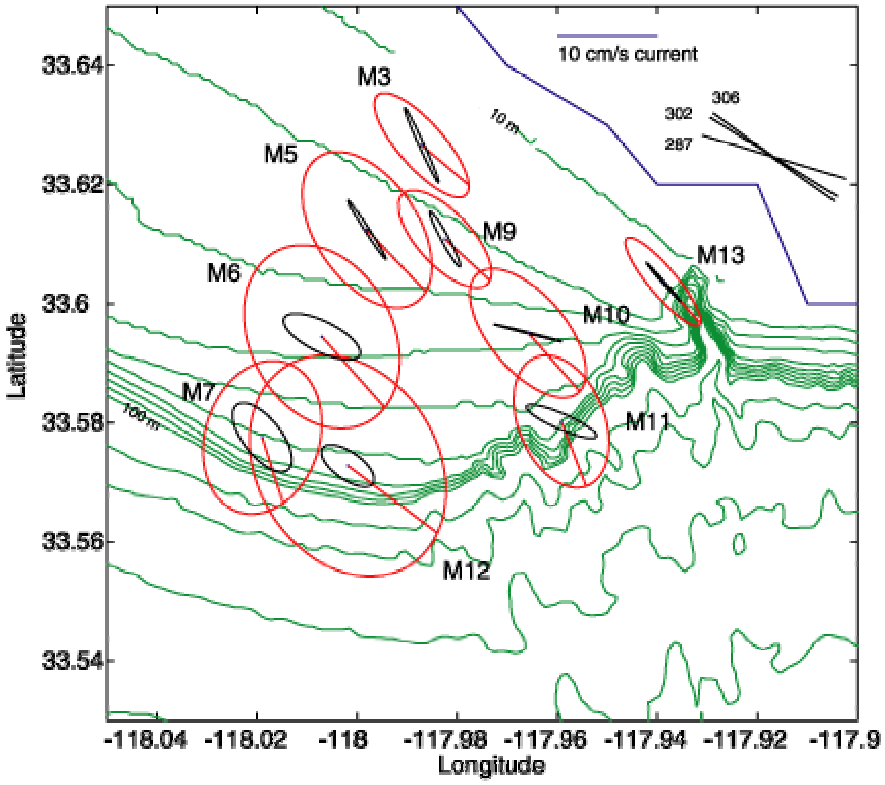

Figure 8. Diurnal (red) and semi-diurnal (black) near-surface ellipses. Phases of diurnal ellipse indicated by red line. Alongshore direction is 306°, alongshelf direction for M3, M5, M6, M7, M9, and M13 is 302°, alongshelf direction for M10, M11, and M12 is 287°. Contour intervals are 10 m until 100 m depth, and 20 m after that. Ocean current speed scale indicated by blue line at top of figure.

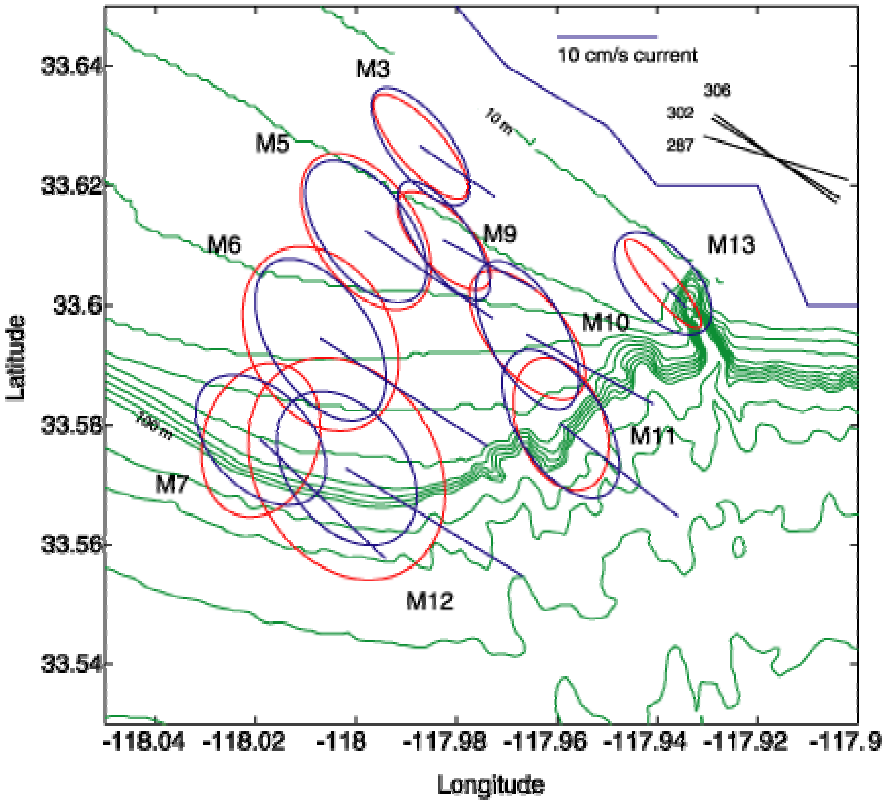

Figure 9. Diurnal (red) and principal axes (blue) near-surface ellipses. Mean speed and direction of currents indicated by blue line from center of each ellipse. Alongshore and alongshelf directions and contour intervals same as Figure 8. Ocean current speed scale indicated by blue line at top of figure.

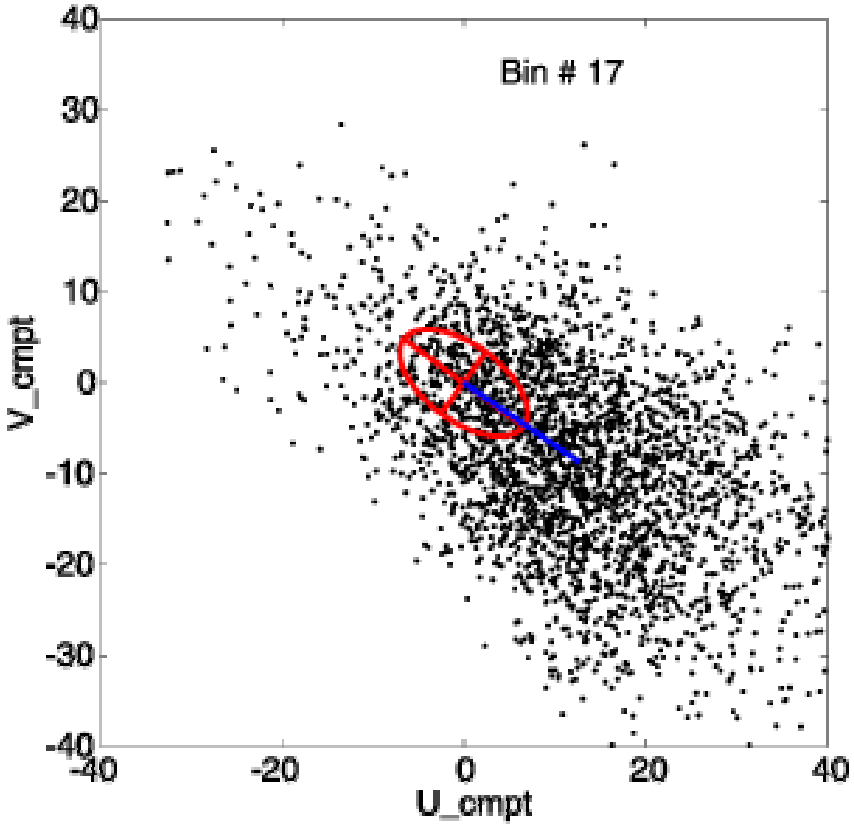

Figure 10. Principal axes ellipse (red), mean velocity vector (blue) and velocity scatter plot for M5 (depth 6 m).

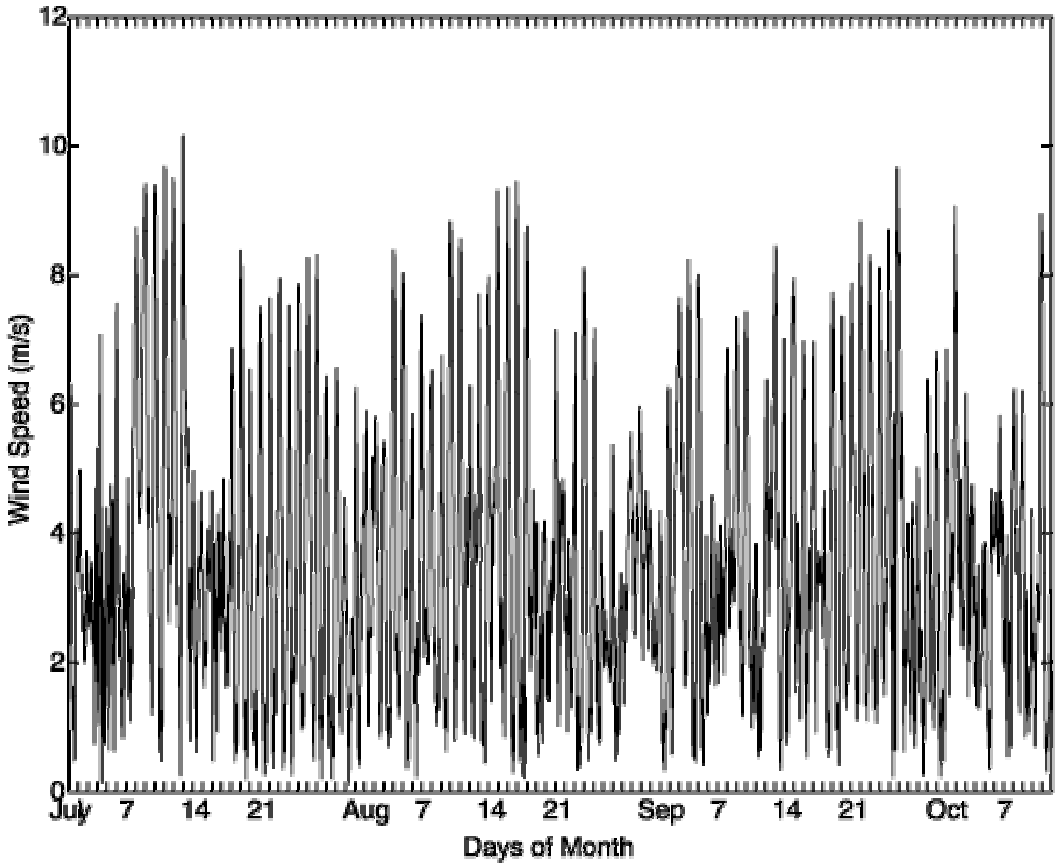

Figure 11. Time series of wind speed at M7.

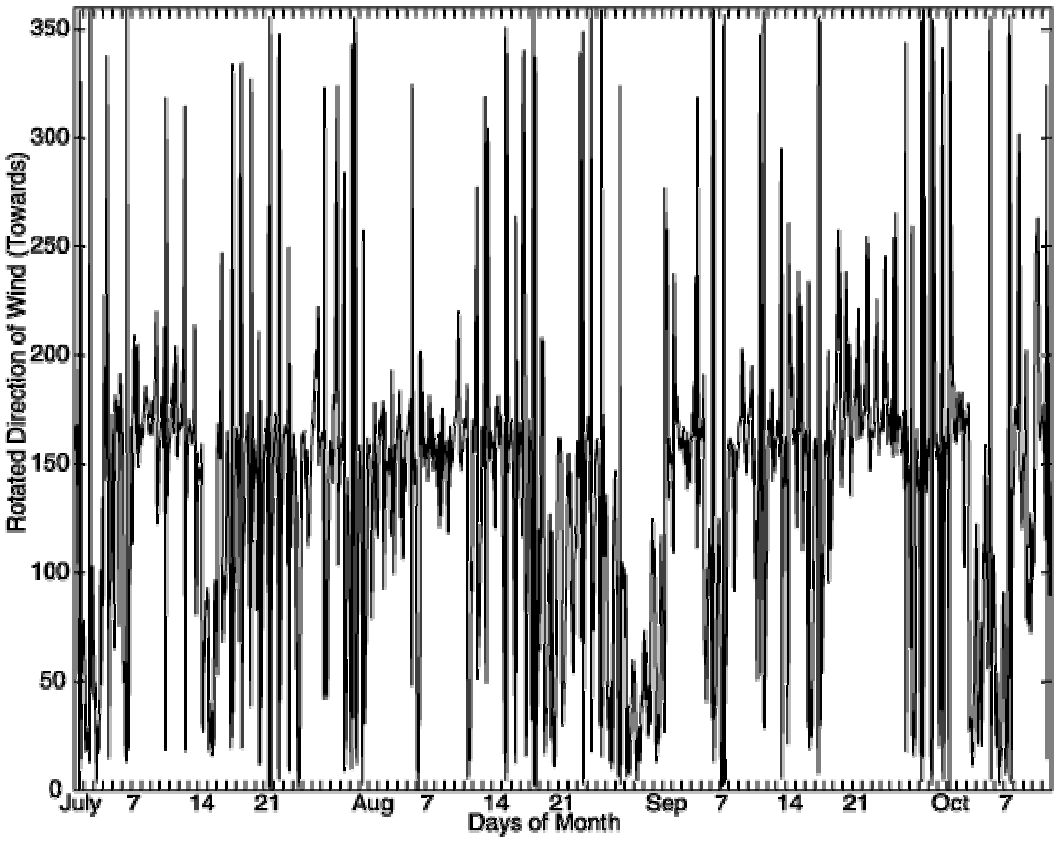

Figure 12. Rotated direction of wind at M7. 0^{o} on the y-axis corresponds to the upcoast alongshelf direction, 306^{o}, and 180^{o} corresponds to the downcoast alongshelf direction, 126^{o}.

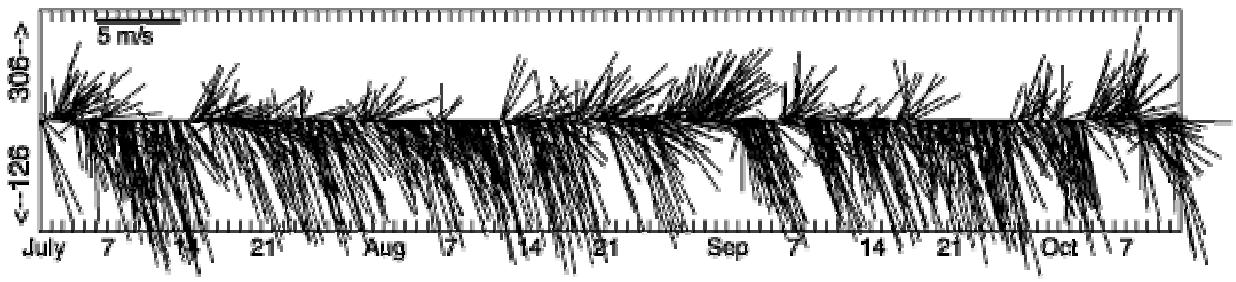

Figure 13. Stick plot of winds measured from surface buoy at M7. Sticks point from the x-axis towards the direction in which the wind is blowing. The alongshore upcoast direction (306^{o}) is up on the page.

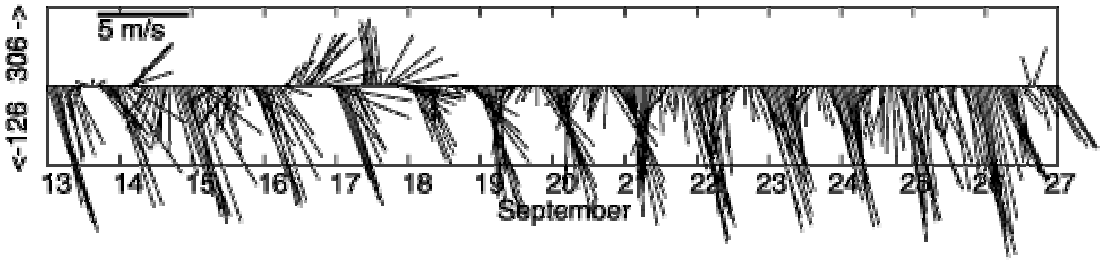

Figure 14. Stick plot of wind from Sept 13-27, 2001. 306^{o}, the upcoast alongshore direction, is up on the page. Days are in GMT, beginning of day corresponds to 1700 PDT.

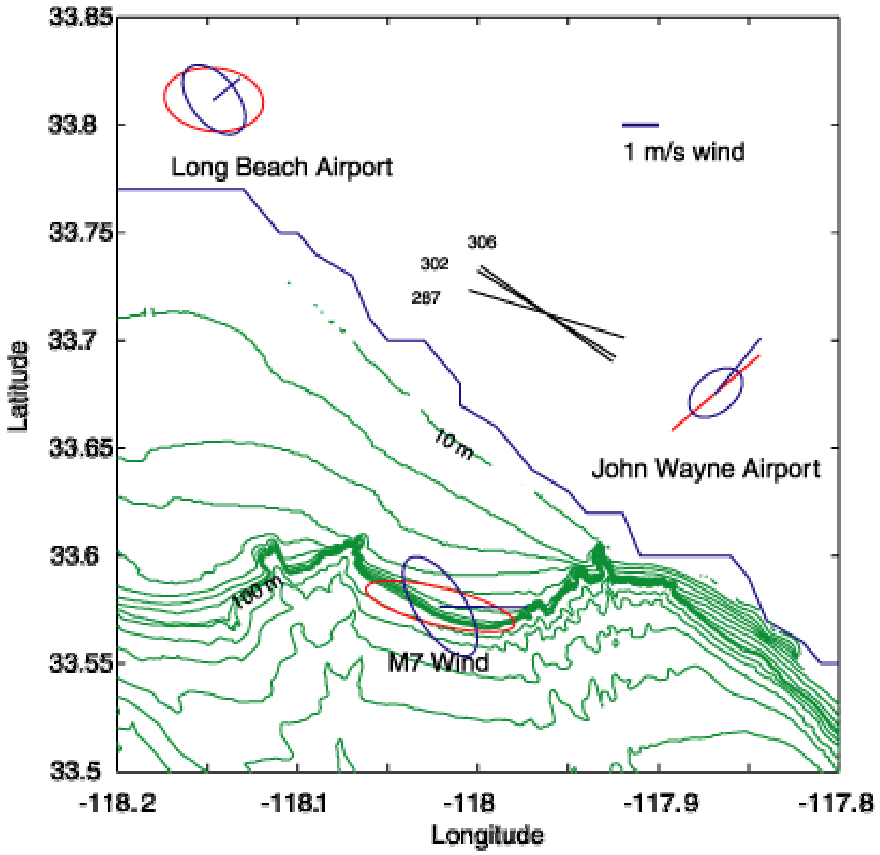

Figure 15. Diurnal (red) and principal axes (blue) wind ellipses. Mean speed and direction of wind indicated by blue line from center of each ellipse. Wind speed scale indicated by blue line. Alongshore and alongshelf directions and contour intervals same as Figure 8.

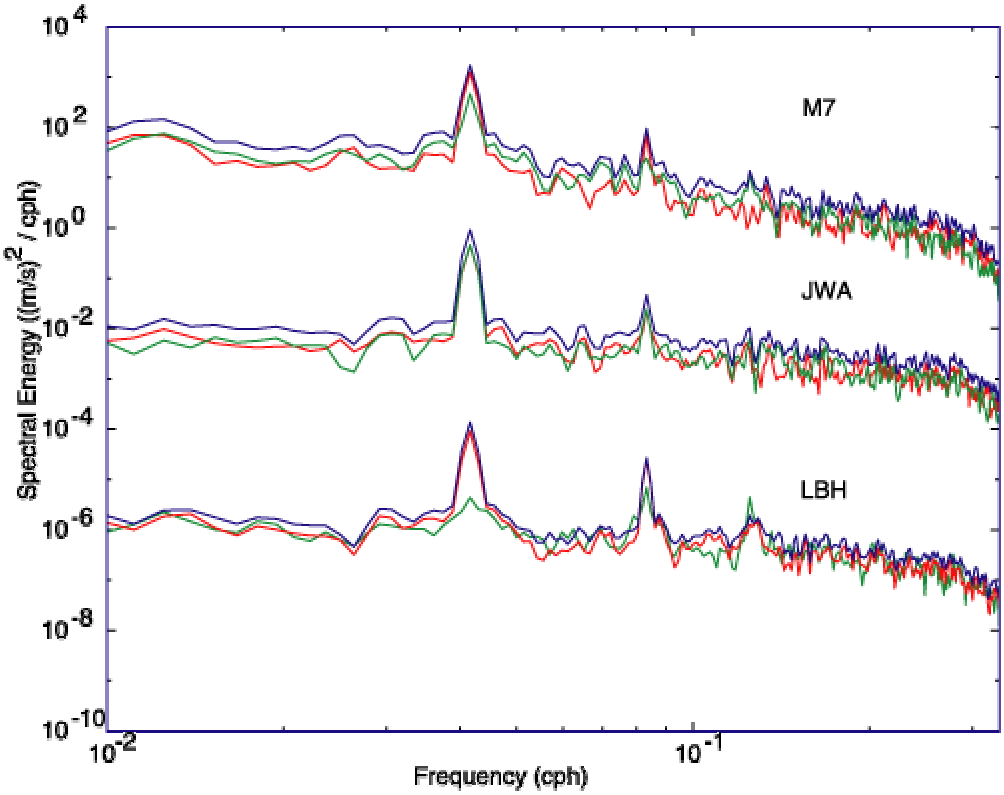

Figure 16. Rotary spectra for wind at M7 (top), JWA (middle), and LBH (bottom). Red represents CW energy, green represents CCW energy, and blue represents the sum of the two. Offset between spectra is 10^{-4}.

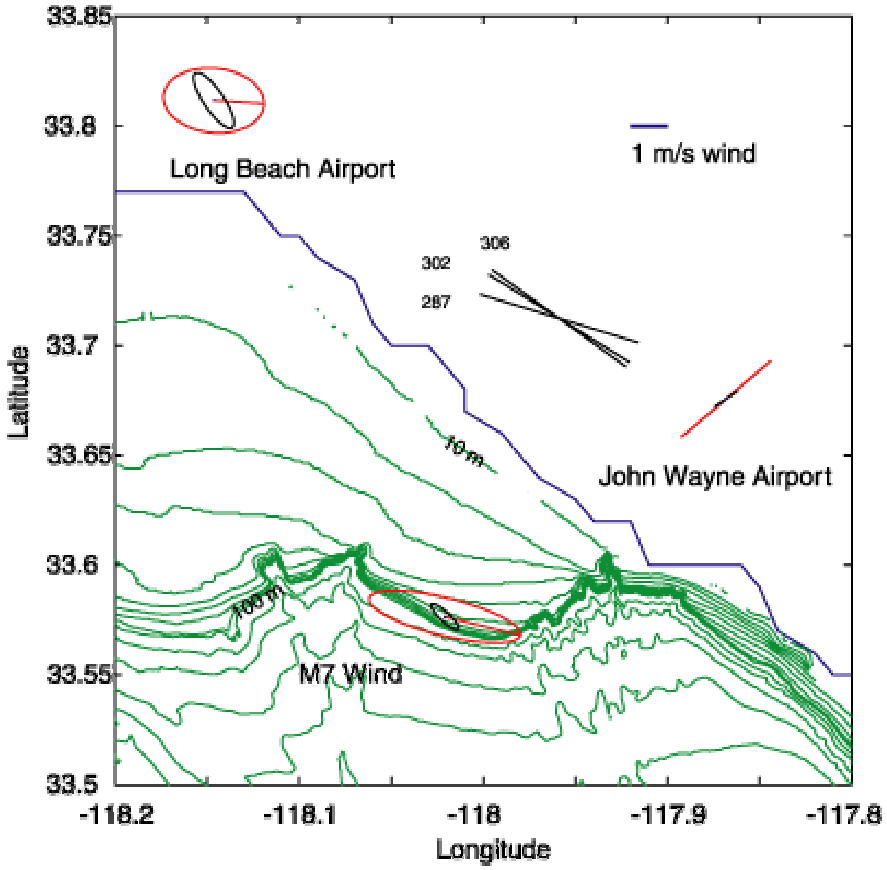

Figure 17. Diurnal (red) and semi-diurnal (black) wind ellipses. Phase of diurnal ellipse indicated by red line. Wind speed scale indicated by blue line. Alongshore and alongshelf directions and contour intervals same as Figure 8.

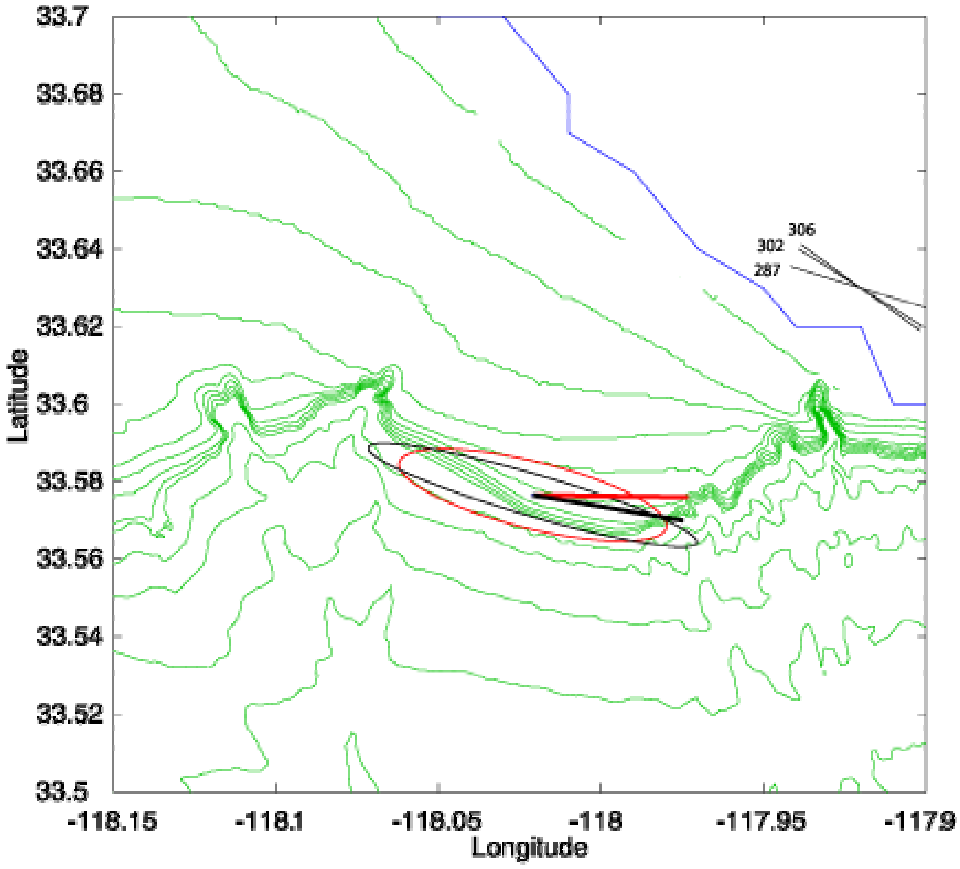

Figure 18. Diurnal ellipses of wind (red) and wind stress (black) at M7. Alongshore and alongshelf directions and contour intervals same as Figure 8. The mean wind speed (red line) and wind stress (black line) are 2.39 m/s and 0.0235 N/m^2, respectively.

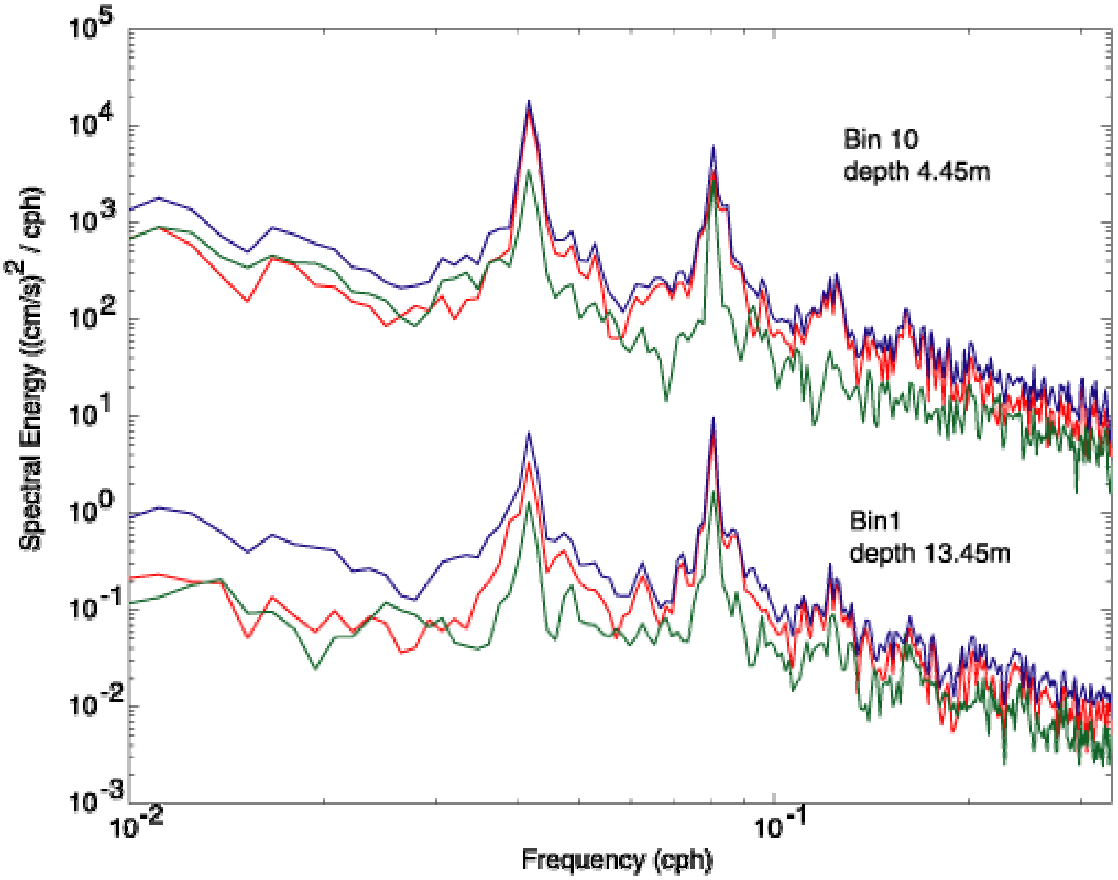

Figure 19. Rotary spectra for near-surface and near-bottom currents at M3. Red represents CW energy, green represents CCW energy, and blue represents the sum of the two. Offset between spectra is 10^{-4}.

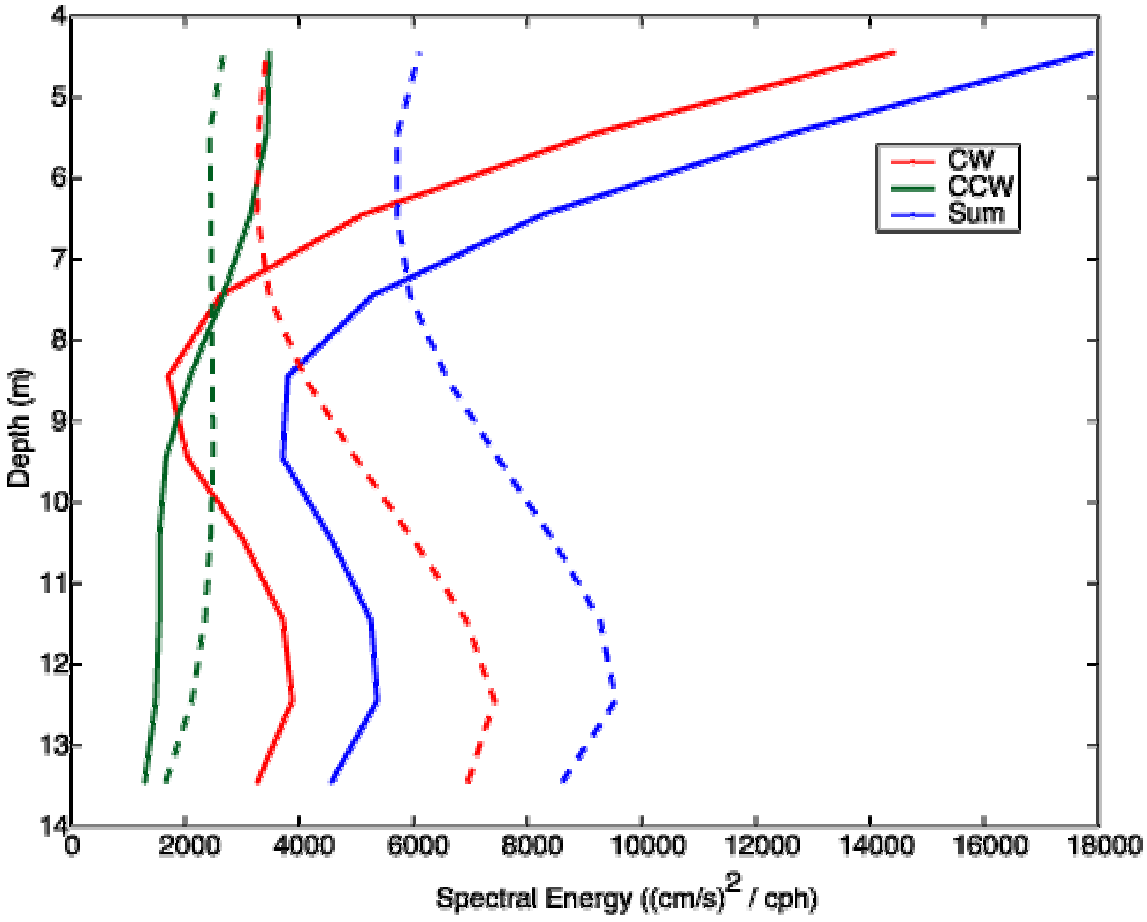

Figure 20. Diurnal (solid) and semi-diurnal (dashed) energy with depth at M3. Red represents CW energy, green represents CCW energy, and blue represents the sum of the two.

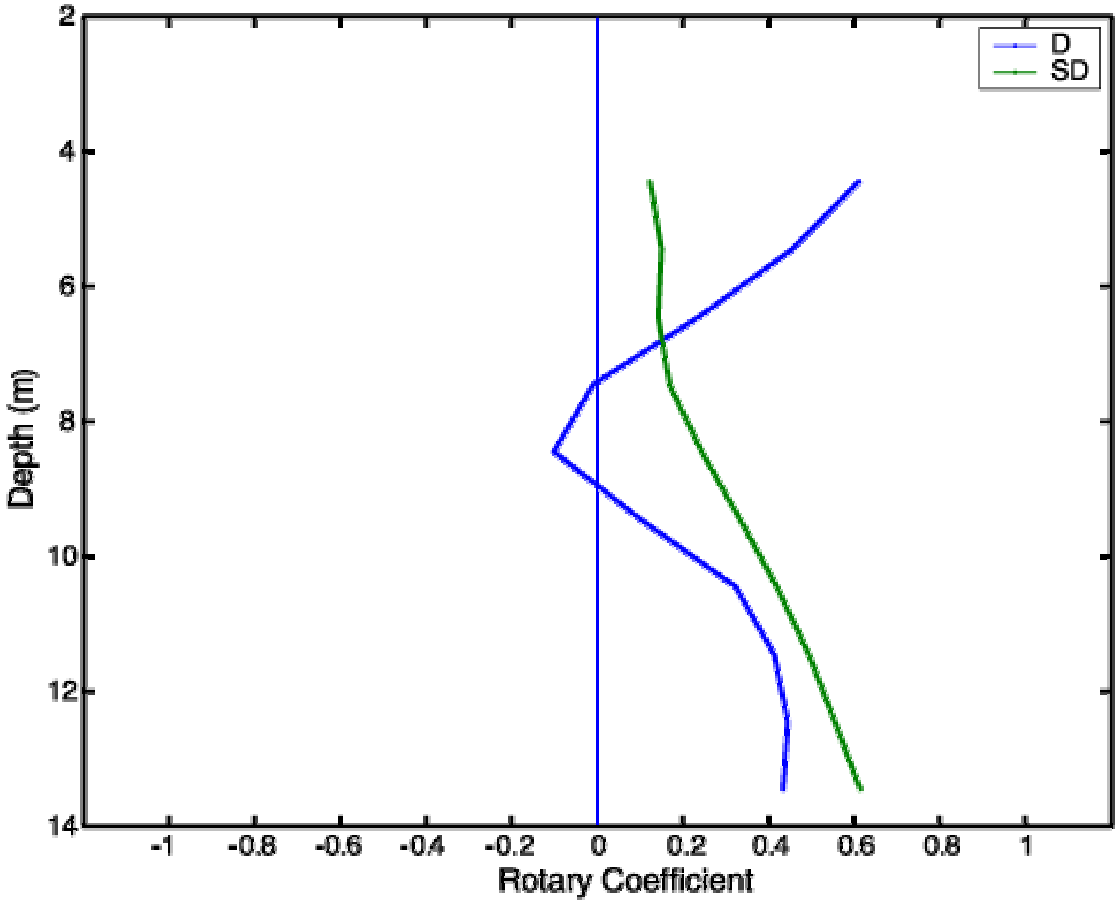

Figure 21. Diurnal (blue) and semi-diurnal (green) rotary coefficients for M3.

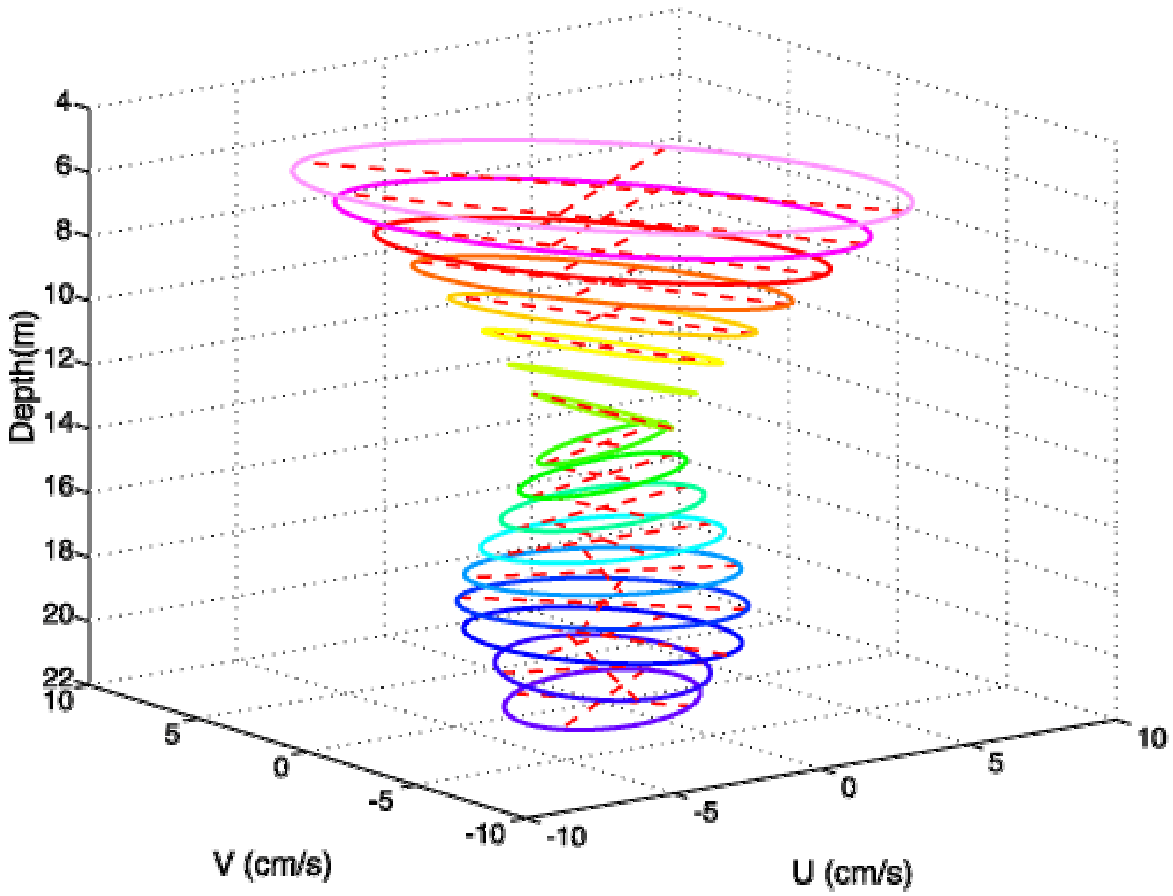

Figure 22. Diurnal ellipses with depth for M5.

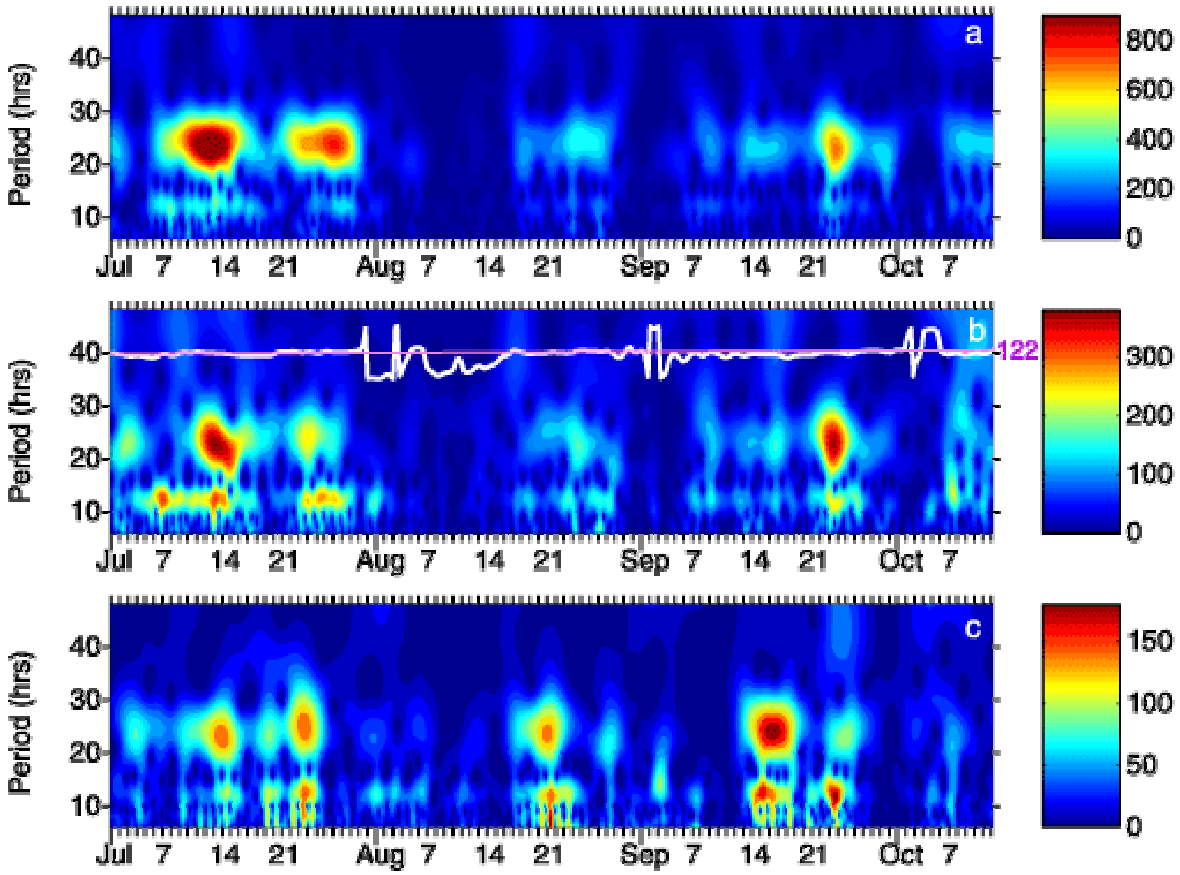

Figure 23. Continuous wavelet transform (CWT) of kinetic energy at M6 at a) 3 m, b) 9 m, and c) 30 m depth. White line in b) represents the direction toward which the 40-hr low-pass currents at 10 m depth are flowing, range is from 0^{o} to 360^{o}. Pink line represents the downcoast alongshelf direction, 122^{o}. Note that the scale for the color bar differs between panels.

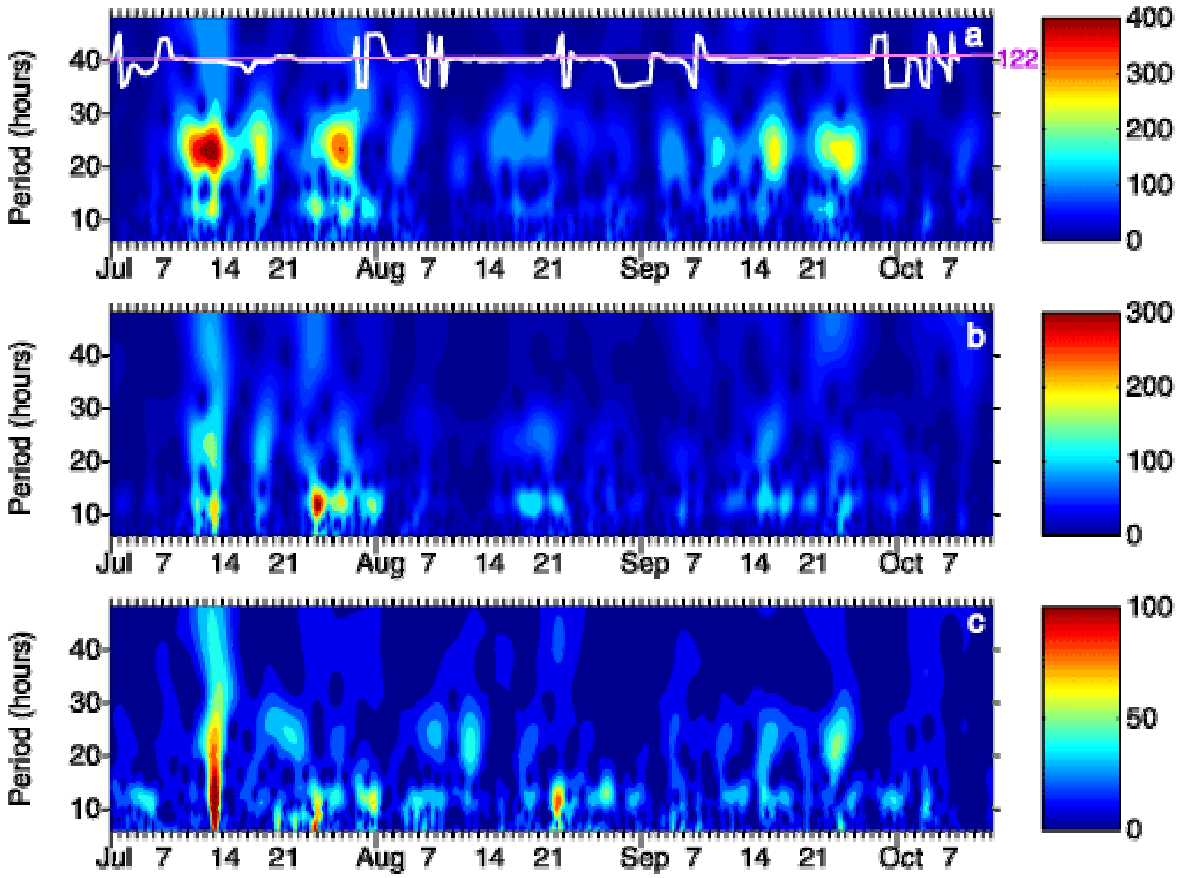

Figure 24. Continuous wavelet transform (CWT) of kinetic energy at M3 at a) 4 m, b) 9 m, and c) 13 m depth. White line in a) represents the direction toward which the 40-hr low-pass currents at 4 m depth are flowing, range is from 0^{o} to 360^{o}. Pink line represents the downcoast alongshelf direction, 122^{o}. Note that the scale for the color bar differs between panels.

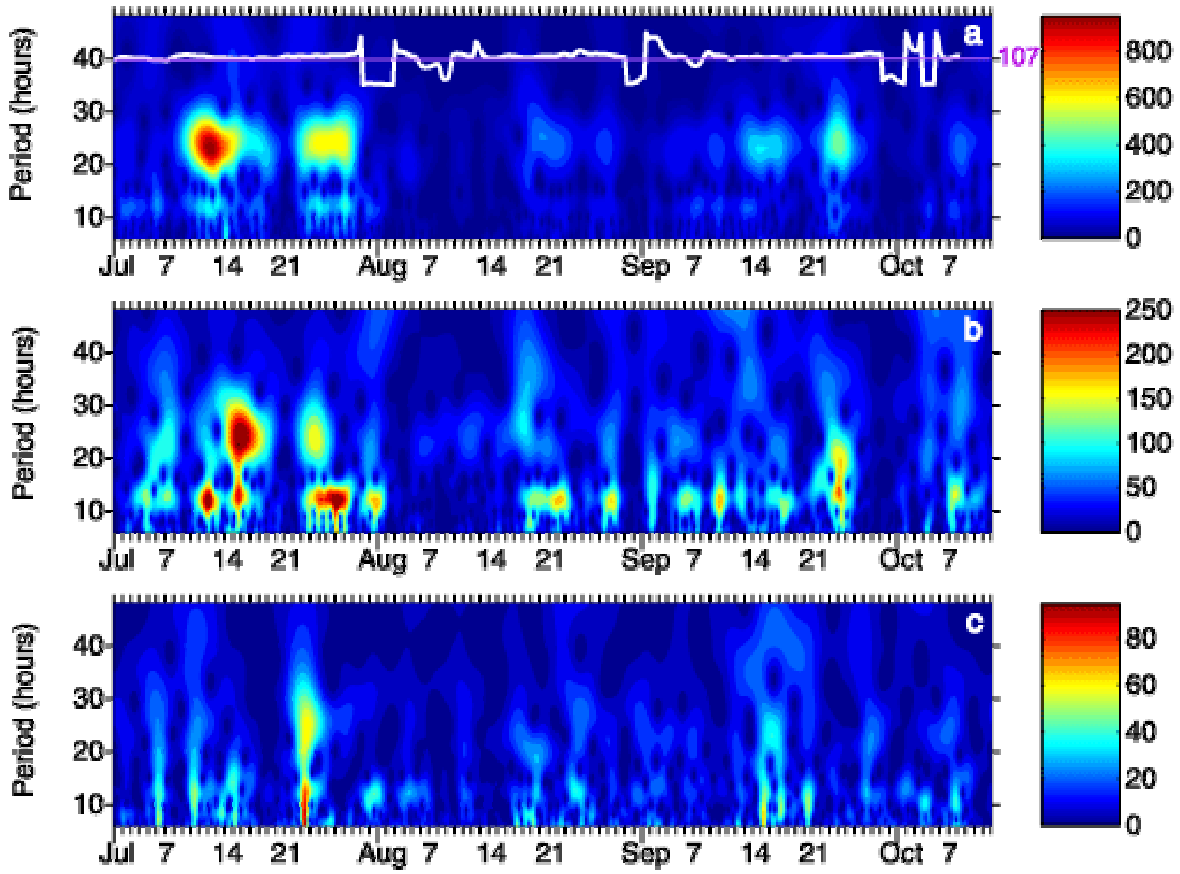

Figure 25. Continuous wavelet transform (CWT) of kinetic energy at M10 at a) 6 m, b) 14 m, and c) 32 m depth. White line in a) represents the direction toward which the 40-hr low-pass currents at 6 m depth are flowing, range is from 0^{o} to 360^{o}. Pink line represents the downcoast alongshelf direction, 107^{o}. Note that the scale for the color bar differs between panels.

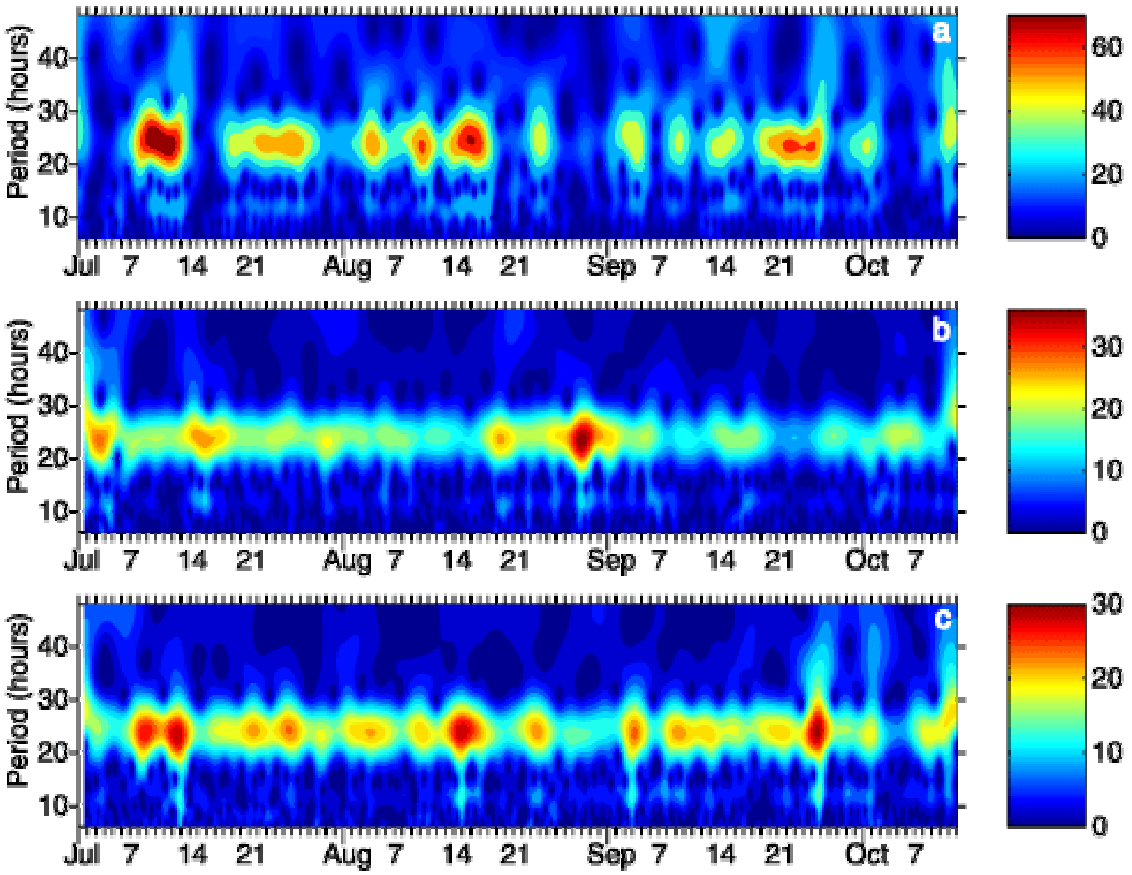

Figure 26. CWT for kinetic energy of winds measured at a) M7, b) JWA, and c) LBH.

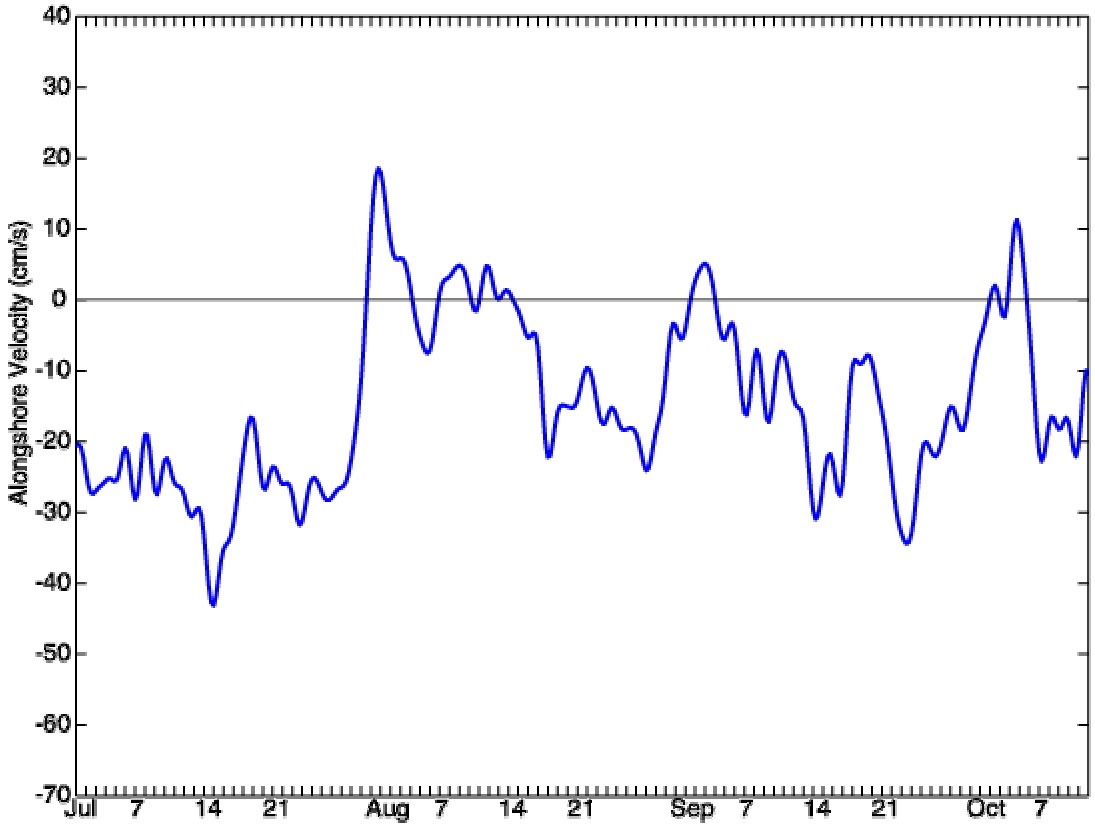

Figure 27. Alongshore velocity (positive towards 302^{o}) of 10 m low-pass filtered currents at M6.

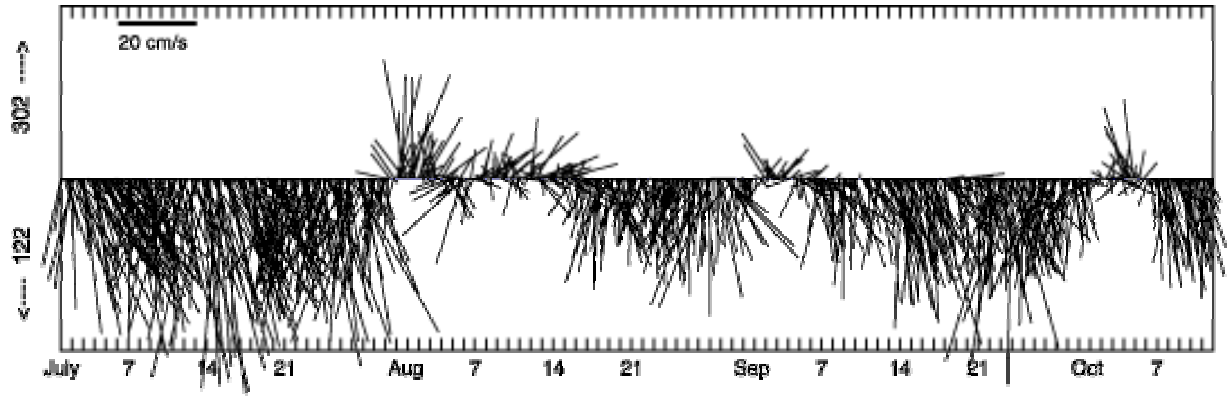

Figure 28. Stick plot of 10 m currents at M6. The upcoast alongshelf direction, 302^{o}, is up on the page.

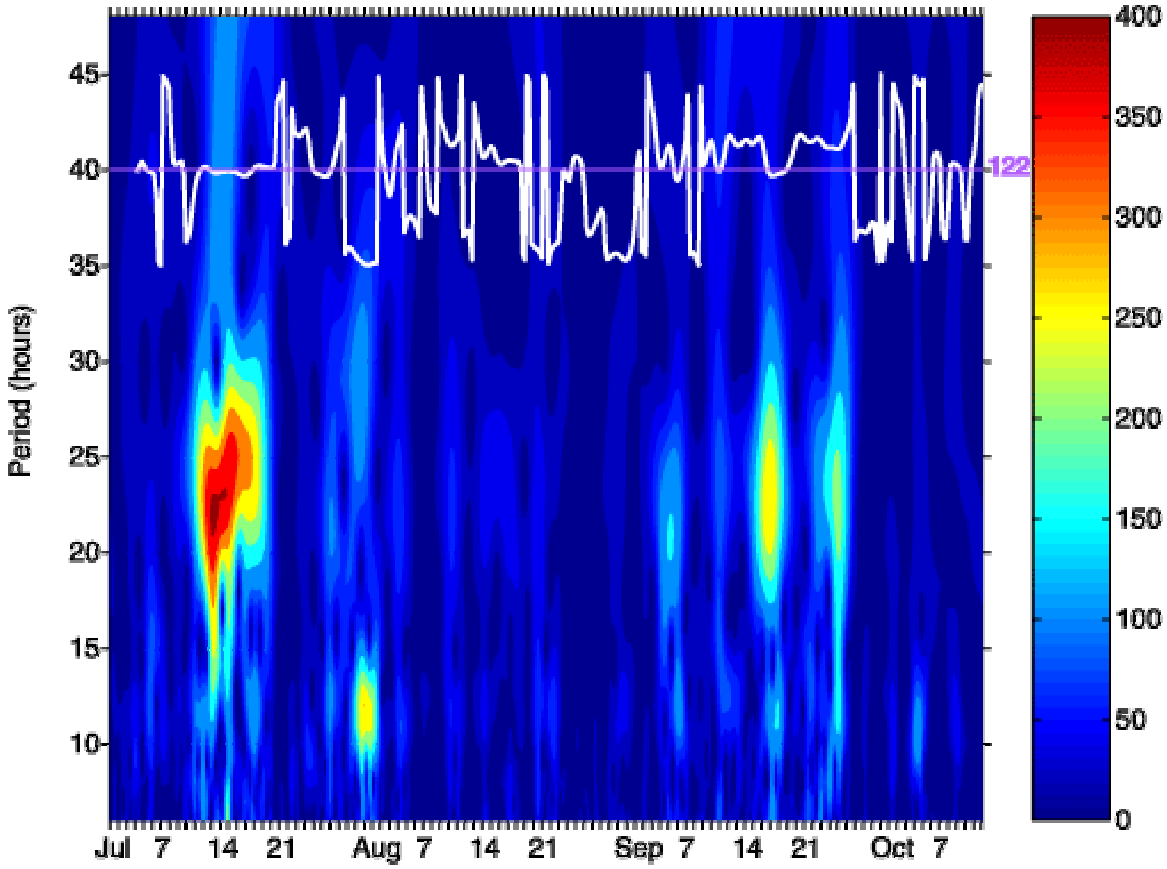

Figure 29. Continuous wavelet transform (CWT) of kinetic energy at M13 at 5 m depth. White line represents the direction toward which the 40-hr low-pass currents at 5 m depth are flowing, range is from 0^{o} to 360^{o}. Pink line represents the downcoast alongshelf direction, 122^{o}.

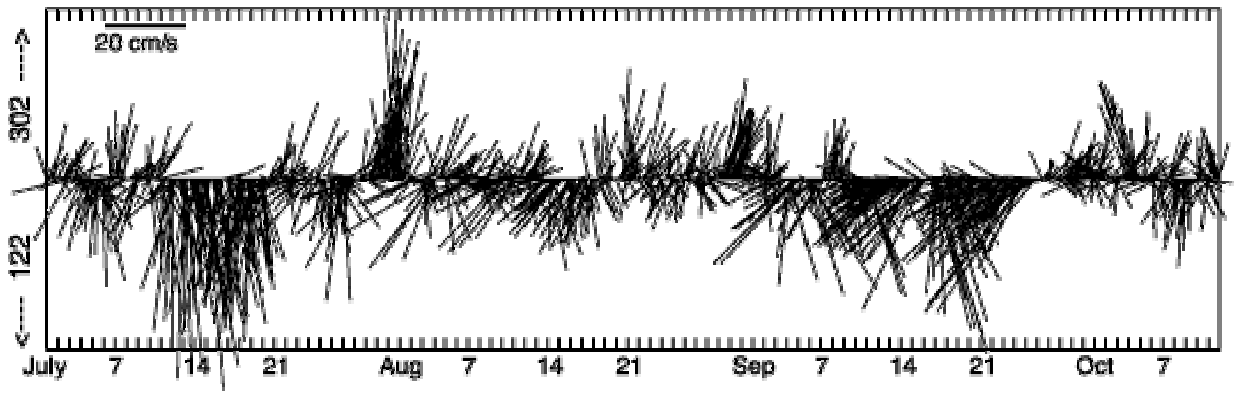

Figure 30. Rotated 5 m currents at M13. 302^{o} is upcoast alongshelf, and 122^{o} is downcoast alongshelf.

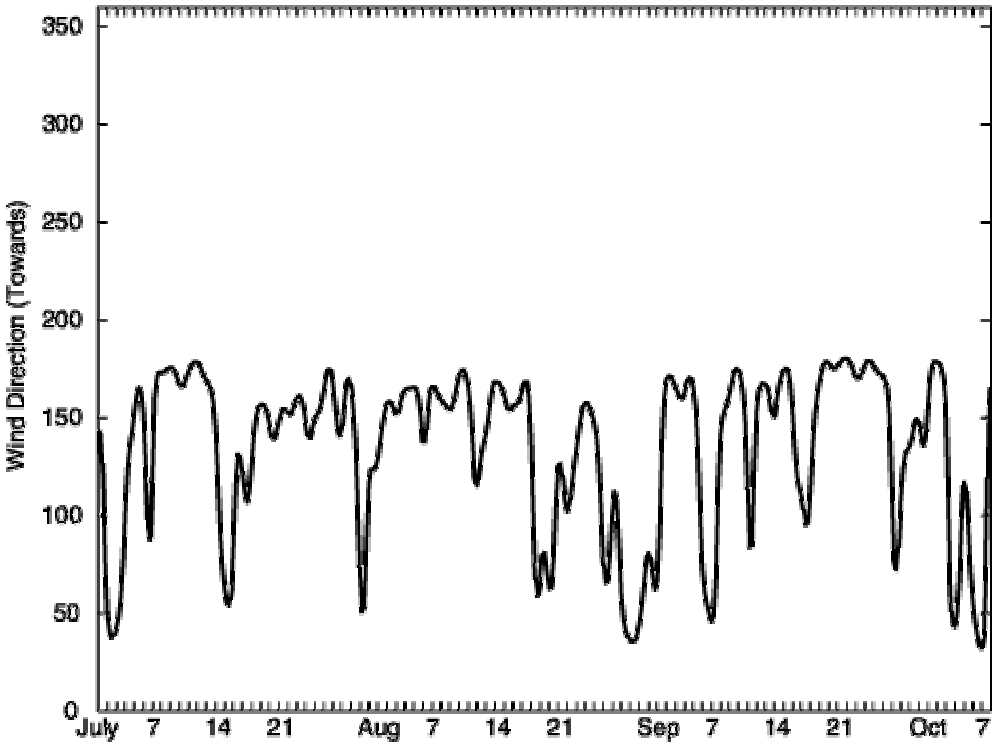

Figure 31. 40-HLP rotated wind direction (toward) at M7. 180^{o} is downcoast alongshelf direction.

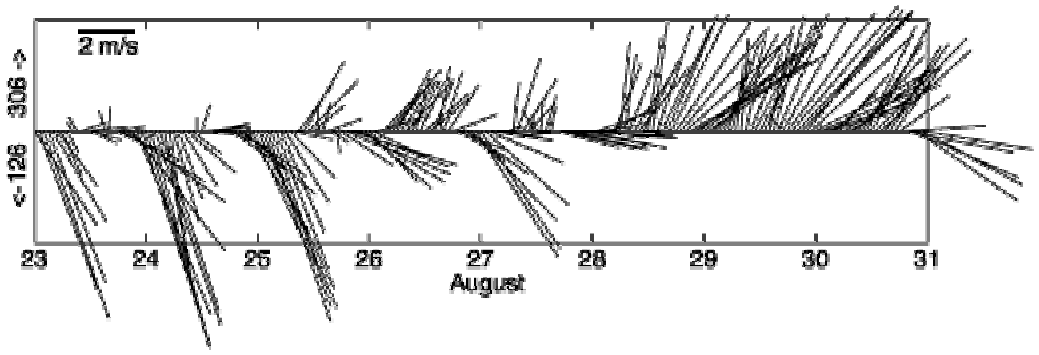

Figure 32. Stick plot of wind from August 23-31, 2001. The upcoast alongshore direction, 306^{o} is up on the page. Days are in GMT, beginning of day corresponds to 1700 PDT.

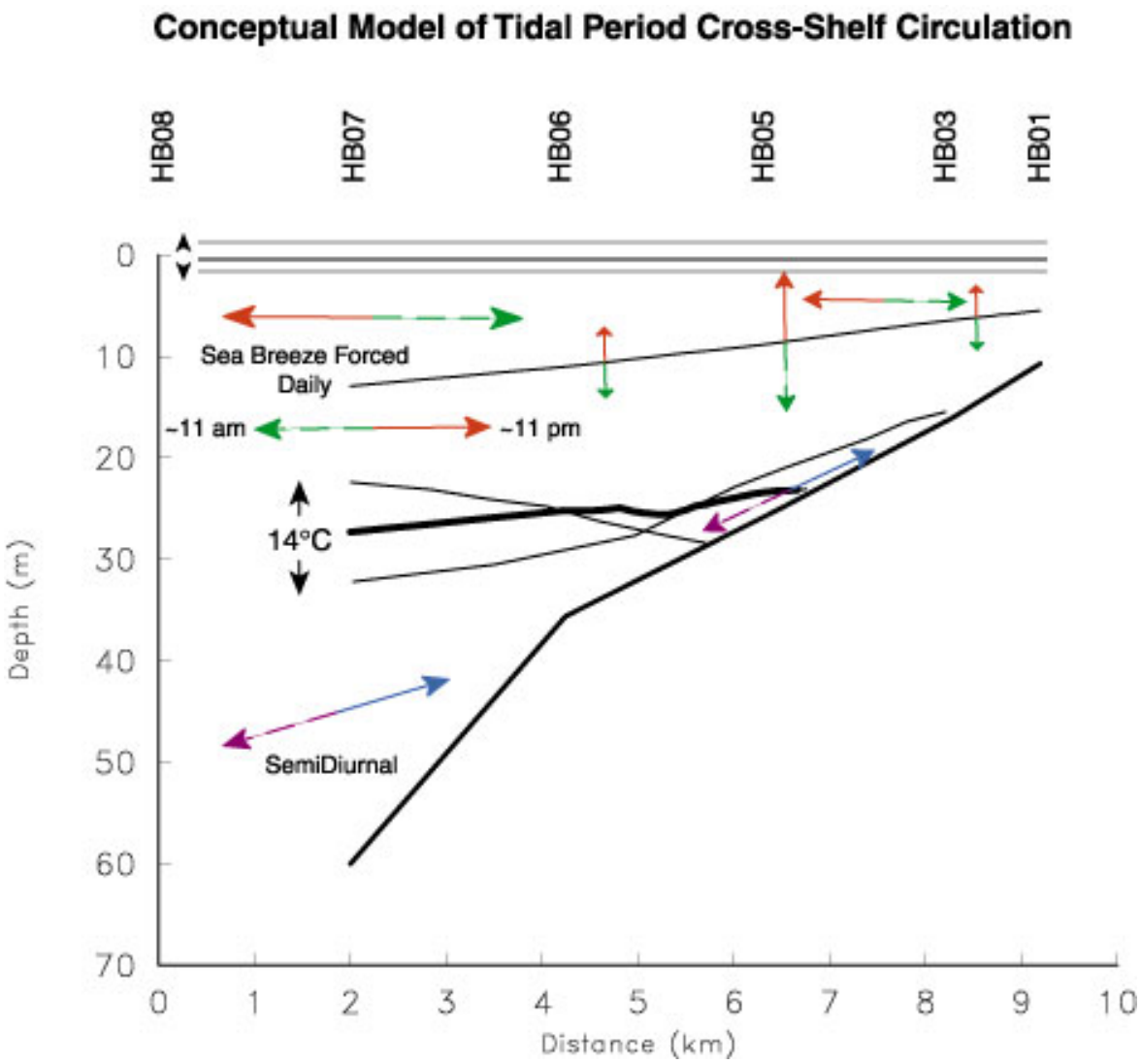

Figure 33. Conceptual model of tidal period circulation (from Noble and Hamilton, 2003). Solid and dashed arrows represent maximum velocities a half-cycle apart. Red and green, and blue and purple arrows, are 24 and 12.42 hour oscillations, respectively.

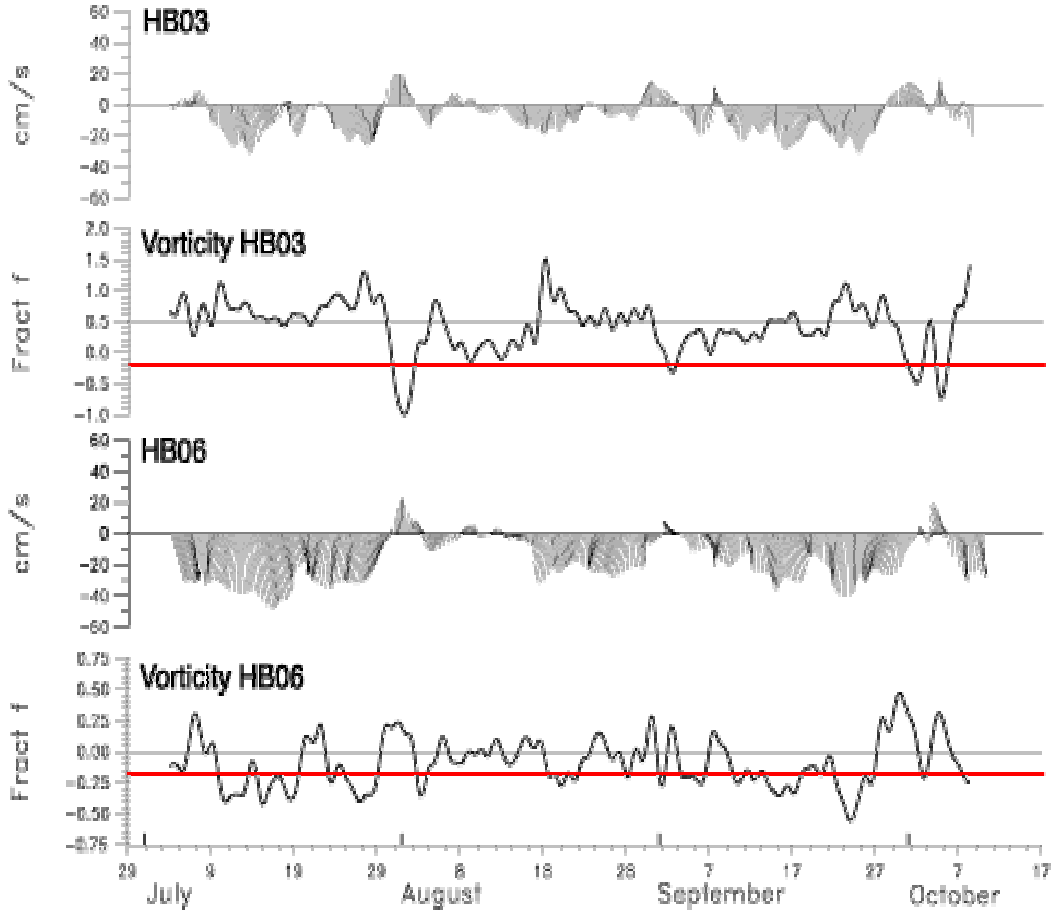

Figure 34. Time series of relative vorticity (normalized by f) and the 40 HLP current vectors at 5 m depth at M3 and M6. The red lines denote the value for ζ / f (= –0.18), below which diurnal waves can propagate (adapted from Hamilton, 2003).

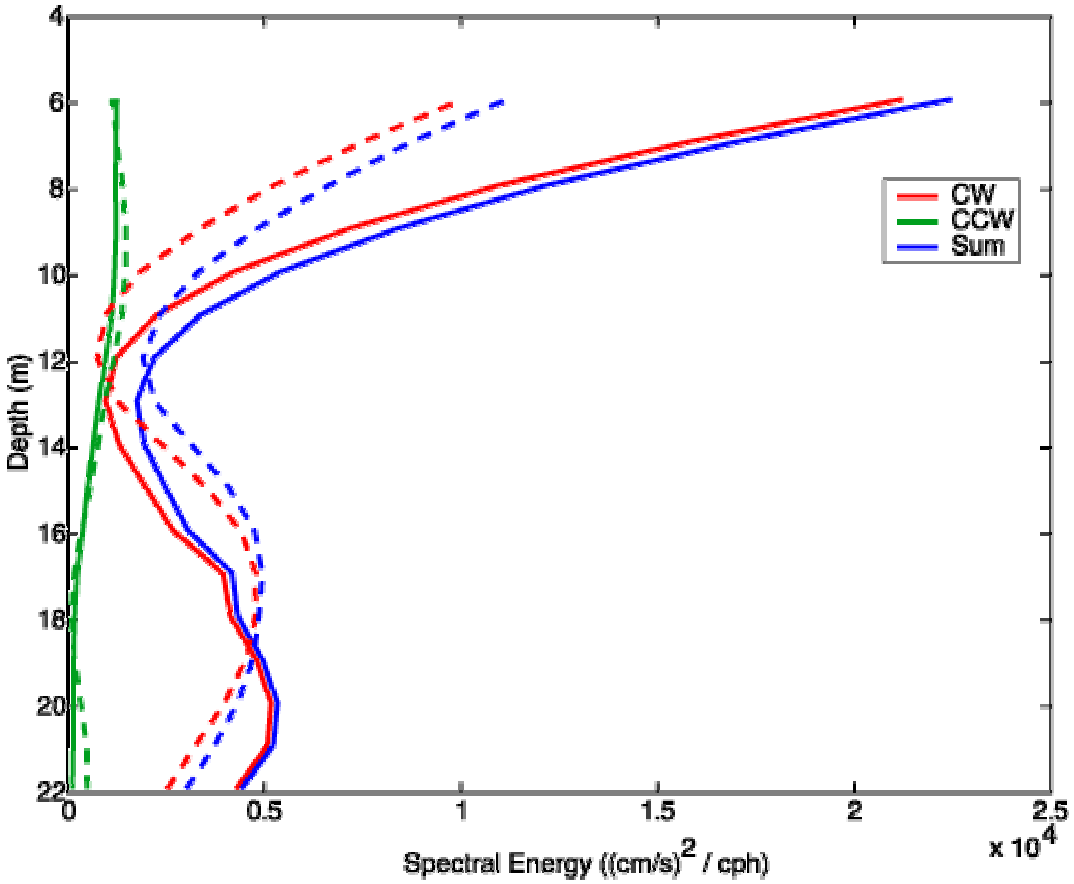

Figure 35. Diurnal energy with depth at M5. Freely propagating internal waves of diurnal period are possible July 9-21 (solid line), and are not possible August 9-21 (dashed line).

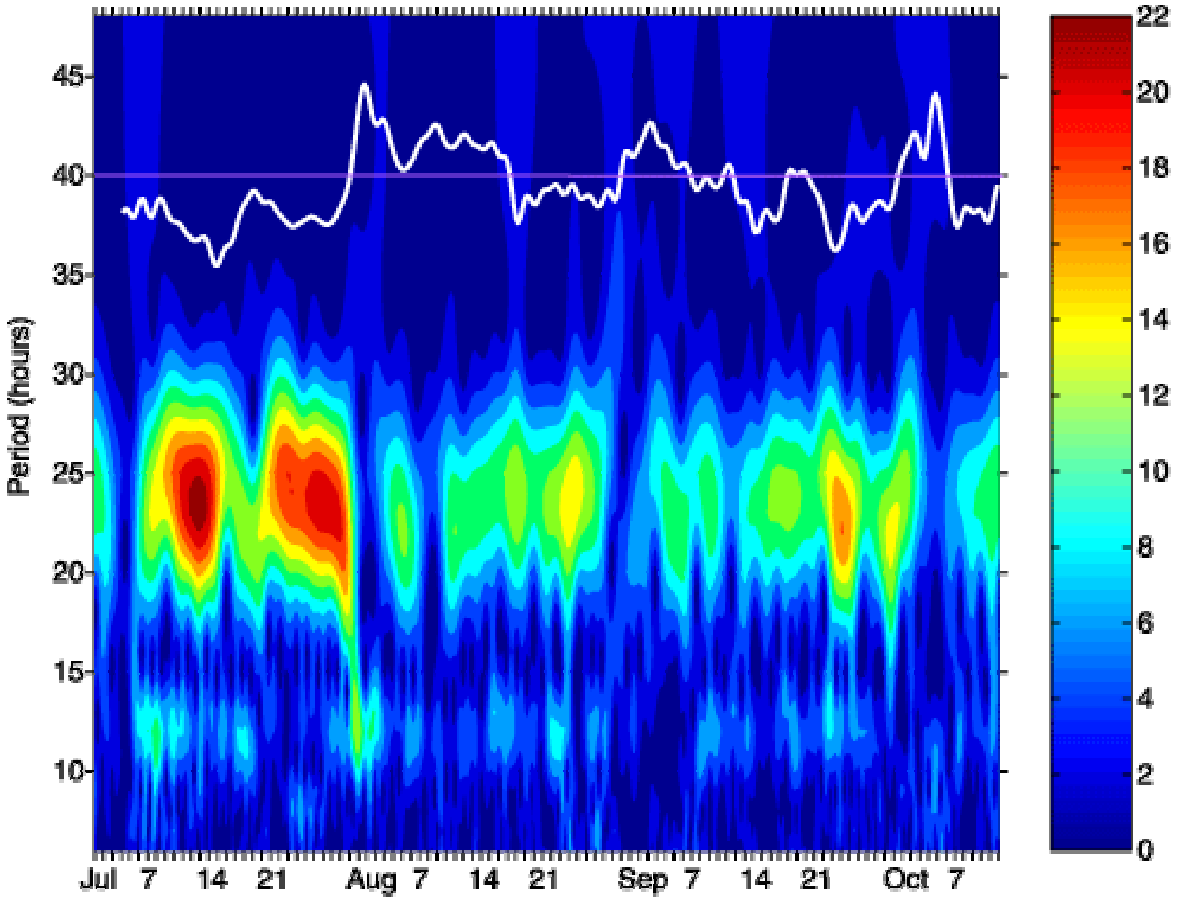

Figure 36. CWT for along-ellipse ocean currents at M6 (depth 3 m). Along-ellipse direction is 332°. White line represents 40-hlp alongshelf currents at 10 m (positive towards 302°). Pink line represents 0.

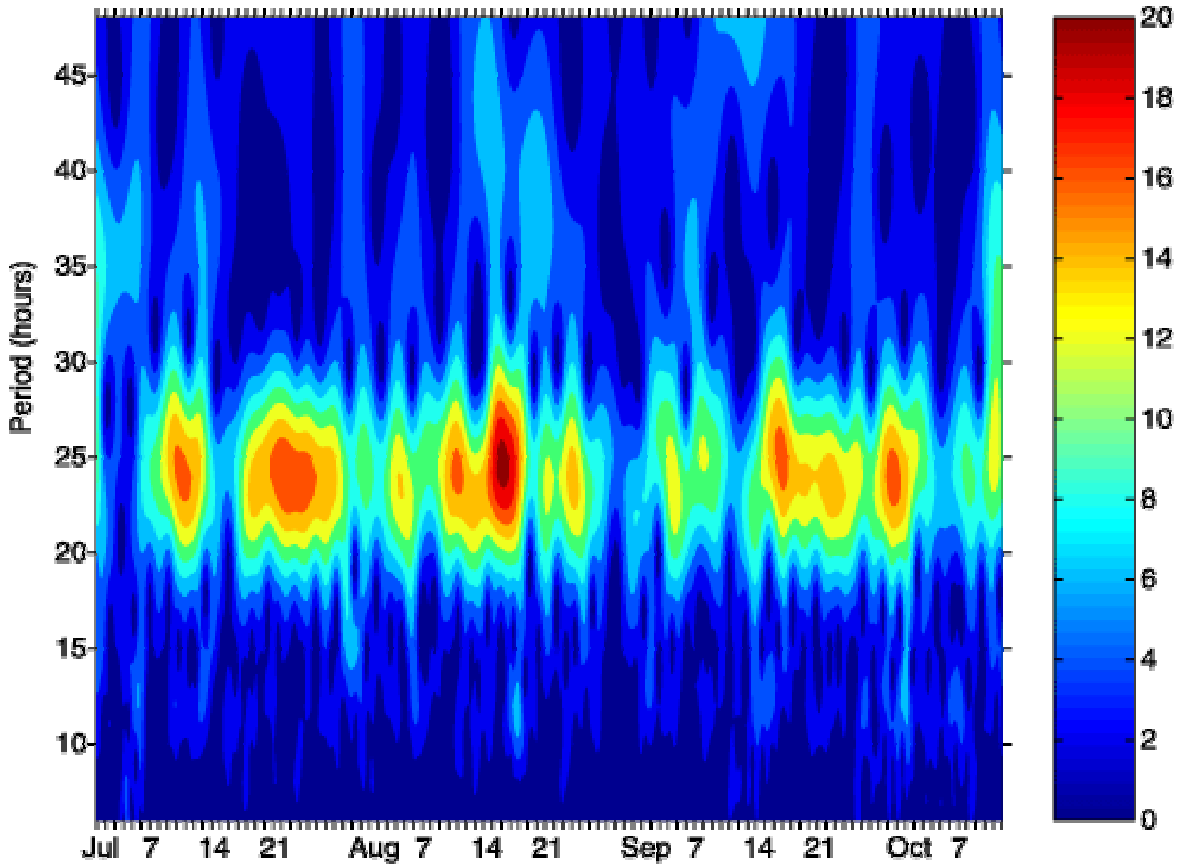

Figure 37. CWT for along-ellipse wind at M7. Along-ellipse direction is 284^{o}.

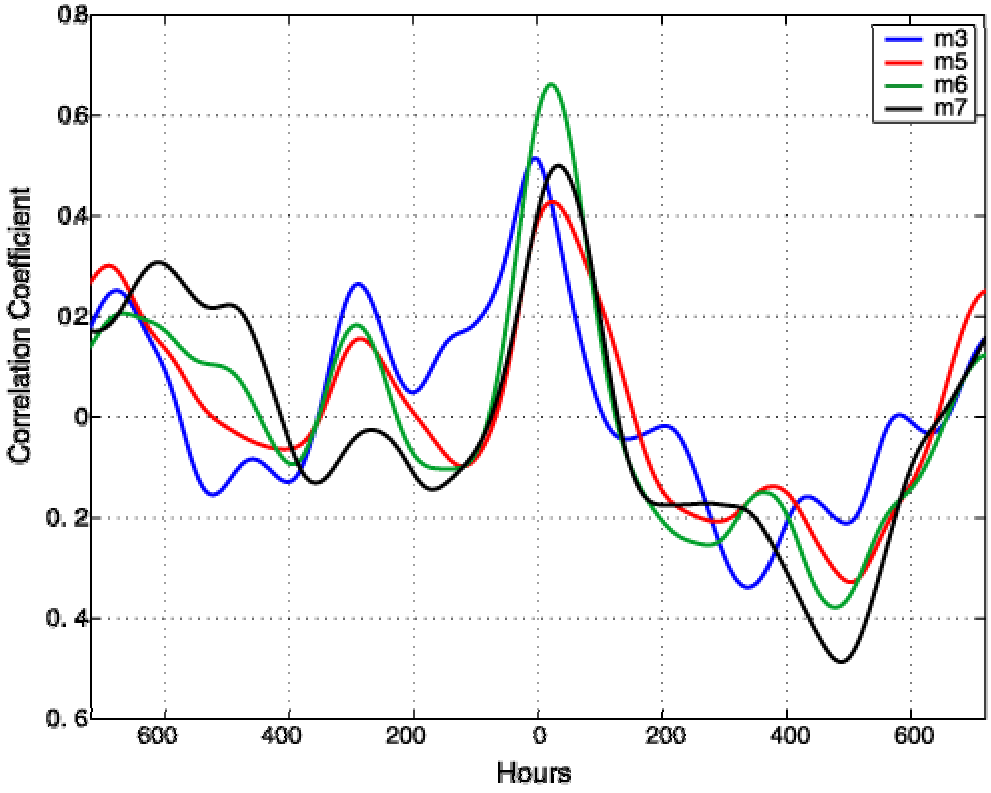

Figure 38. Correlation between M7 along-ellipse winds and M3 (blue), M5 (red), M6 (green), and M7(black) along-ellipse near-surface ocean currents.

LIST OF REFERENCES

Beardsley, R.C., C.E. Dorman, C.A. Friehe, L.K. Rosenfeld, and C.D. Winant, Local atmospheric forcing during the Coastal Ocean Dynamics Experiment. 1. A description of the marine boundary layer and atmospheric conditions over a Northern California upwelling region, *J. Geophys. Res*., 92 (C2), 1467-1488, 1987.

Bray, N.A., A. Keyes, and W.M.L. Morawitz, The California Current System in the Southern California Bight and the Santa Barbara Channel, *J. Geophys. Res*., 104 (C4), 7695-7714, 1999.

Emery, W.J., and R.E. Thomson, Data Analysis Methods in Physical Oceanography. Kentucky: Gray Publishing, 1997.

Gill, A.E., Atmosphere Ocean Dynamics, Orlando: Academic Press Inc., 1982.

Hamilton, P., J.J. Singer, E. Waddell, and G. Robertson, Circulation processes on the San Pedro Shelf, Proceeding: MTS 2001 Conf., November 2001, Honolulu, Hawaii.

Hamilton, P., Seabreeze, Ch. 5 in Huntington Beach Shoreline Contamination Investigation, Phase III, Draft Final Report. Prepared for OCSD, 2003.

Hickey, B.M., Circulation over the Santa Monica-San Pedro Basin and shelf, *Prog. Oceanogr*, 30 (C9), 37-115, 1992.

Hickey, B.M., Coastal oceanography of western North America from the tip of Baja California to Vancouver Island, in *The Sea: The Global Coastal Ocean: Regional Studies and Syntheses*, vol. 11, edited by A.R. Robinson and K.H. Brink, chap. 12, pp. 345-393, John Wiley, New York, 1998.

Hickey, B.M., E.L. Dobbins, and S.E. Allen, Local and remote forcing of currents and temperature in the central southern California bight, *J. Geophys Res*., in press, 2003.

Hickey, B.M., and N. E. Pola, The seasonal alongshore pressure gradient on the west coast of the United States, *J. Geophys. Res*., 88 (C12), 7623-7633, 1983.

Hubbard, B.B. The World According to Wavelets. Wellesley: A K Peters, 1996.

Jones, B., P. Hamilton, J. Largier, M. Noble, L. Rosenfeld, and J. Xu, Methodology, Ch. 9 in Huntington Beach Shoreline Contamination Investigation, Phase III, Draft Final Report. Prepared for OCSD, 2003.

Large, W.S., and S. Pond, Open ocean momentum flux measurements in moderate to strong winds, *J. Phys. Oceanogr.*, 11, 324-336, 1981.

Lerczak, J.A., M.C. Hendershott, and C.D. Winant, Observations and modeling of coastal internal waves driven by a diurnal sea breeze, *J. Geophys. Res*., 106 (C9), 19,715-19,729, 2001.

Lynn, R.J, and J. J. Simpson, The California Current System: The seasonal variability of its physical characteristics, *J. Geophys. Res*., 92(C12), 12,947-12,966, 1987.

McCreary, J.P., P. K. Kundu, and S. Y. Chao, On the dynamics of the California Current System, *J. Mar. Res*., 45, 1-32, 1987.

Noble, M. and P. Hamilton, Tidal transport pathways, Ch. 6 in Huntington Beach Shoreline Contamination Investigation, Phase III, Draft Final Report. Prepared for OCSD, 2003.

Noble, M., P. Hamilton, B. Jones, J. Largier, K. Orzech, L. Rosenfeld, J. Xu, Executive summary, Huntington Beach Shoreline Contamination Investigation, Phase III, Draft Final Report. Prepared for OCSD, 2003.

Orange County Sanitation District, Executive Summary, Annual Report 2000, 2001.

Rosenfeld, L. K., Diurnal period wind stress and current fluctuations over the continental shelf off northern California, *J. Geophys. Res*., 93 (C3), 2257-2276, 1988.

SAIC, Strategic Process Study #1: Plume tracking-Ocean currents, Final Report Prepared for OCSD, 61 pp., 2001.

Torrence, C., and G. P. Compo, A practical guide to wavelet analysis, *Bull Amer. Met. Soc.*, 79 (1), 61-78, 1998.

Washburn, L., B.H. Jones, A. Bratkovich, T.D. Dickey, and M.S. Chen, Mixing, dispersion, and resuspension in vicinity of ocean wastewater plume, *J. Hydr. Engr.*, 118 (1), 38-58, 1992.

Winant, C.D., and Clive E. Dorman, Seasonal patterns of surface wind stress and heat flux over the Southern California Bight, *J. Geophys. Res.*, 102 (C3), 5641 -5653, 1997.

Wu, J. Wind-stress coefficients over sea surface near neutral conditions –a revisit, *J. Phys. Oceanogr.*, 10(5), 727-740, 1980.

INITIAL DISTRIBUTION LIST

1. Defense Technical Information Center
   Ft. Belvoir, VA

2. Dudley Knox Library
   Naval Postgraduate School
   Monterey, CA

3. Dr. Leslie Rosenfeld
   Naval Postgraduate School
   Monterey, CA

4. Dr. Carlyle Wash
   Naval Postgraduate School
   Monterey, CA

5. Dr. Kenneth Davidson
   Naval Postgraduate School
   Monterey, CA

6. Dr. Curtis Collins
   Naval Postgraduate School
   Monterey, CA

7. Chairman, Dept. of Oceanography
   Naval Postgraduate School
   Monterey, CA

8. Mr. George Robertson
   Orange County Sanitation District
   Fountain Valley, CA

9. Dr. Marlene Noble
   US Geological Survey
   Menlo Park, CA

10. Dr. Peter Hamilton
    SAIC
    Raleigh, NC

11. Dr. Burton Jones
    University of Southern California
    Los Angeles, CA

12. Dr. John Largier
University of California, San Diego
La Jolla, CA

13. LT Kelly Taylor
Naval Ice Center
Suitland, MD